

# Wavelet Tree Ensembles for Triangulable Manifolds

Hengrui Luo

Department of Statistics, Rice University;

Computational Research Division, Lawrence Berkeley National Laboratory  
and

Akira Horiguchi

Department of Statistics, University of California Davis  
and

Li Ma

Department of Statistics & Data Science Institute, University of Chicago

## Abstract

We develop unbalanced Haar (UH) wavelet tree ensembles for regression on triangulable manifolds. Given data sampled on a triangulated manifold, we construct UH wavelet trees whose atoms are supported on geodesic triangles and form an orthonormal system in  $L^2(\mu_n)$ , where  $\mu_n$  is the empirical measure on the sample, which allows us to use UH trees as weak learners in additive ensembles. Our construction extends classical UH wavelet trees from regular Euclidean grids to generic triangulable manifolds while preserving three key properties: (i) orthogonality and exact reconstruction at the sampled locations, (ii) recursive, data-driven partitions adapted to the geometry of the manifold via geodesic triangulations, and (iii) compatibility with optimization-based and Bayesian ensemble building. In Euclidean settings, the framework reduces to standard UH wavelet tree regression and provides a baseline for comparison. We illustrate the method on synthetic regression on the sphere and on climate anomaly fields on a spherical mesh, where UH ensembles on triangulated manifolds substantially outperform classical tree ensembles and non-adaptive mesh-based wavelets. For completeness, we also report results on image denoising on regular grids. A Bayesian variant (RUHWT) provides posterior uncertainty quantification for function estimates on manifolds. Our implementation is available at <http://www.github.com/hrluo/WaveletTrees>.

*Keywords:* Tree ensemble methods, nonparametric regression, scalar-on-manifold regressions, scalar-on-sphere regressions.

# 1 Introduction

Method / family	Key reference	Domain	Data-driven partition?	Base measure	Ensemble diversity
Dyadic wavelets	<a href="#">Daubechies (1992)</a> <a href="#">Donoho et al. (1995)</a>	Images	No	Lebesgue	None
SHAH	<a href="#">Fryzlewicz &amp; Timmermans (2016)</a>	Images	Yes*	Counting	None
WARP	<a href="#">Li &amp; Ma (2021)</a>	Images	Yes*	Counting	Cyclic spinning
Random Forest	<a href="#">Breiman (2001)</a>	Euclidean	Yes	Empirical	Stochastic splits
BART	<a href="#">Chipman et al. (2010)</a>				
UHWT	<b>This work</b>	Triangulable	Yes	Empirical	None
UHWT boost	<b>This work</b>	Triangulable	Yes	Empirical	Boosting
RRE (with UHWT)	<a href="#">Blaser &amp; Fryzlewicz (2016)</a>	Triangulable	Yes	Empirical	Haar rotations
RotF (with UHWT)	<a href="#">Rodriguez et al. (2006)</a>	Surface	Yes	Empirical	PCA rotations
RotF (with sPCA)	<a href="#">Rodriguez et al. (2006)</a> , <a href="#">Luo et al. (2024)</a>	Sphere	Yes	Empirical	Bootstrap+sPCA

Table 1: Structural properties of classical, adaptive and ensemble wavelet frameworks. \* means that the data-driven part only applies to split dimensions. “Triangulable” refers to “triangulable manifold.” “RotF” is an abbreviation for “Rotation Forest.”

Wavelets are effective for sparsely representing functions with sharp changes and have been broadly applied in scenarios with a low signal-to-noise ratio. This work is motivated by the observation that the existing literature on wavelet regression has largely concerned the effective representation of functions using a set of wavelet bases defined along a single recursive partition tree. At the same time, tree-based regression methods such as Classification and Regression Trees (CART) ([Breiman et al. 1984](#)) have been generalized to ensembles, most notably through random forests ([Breiman 2001](#)) and boosting ([Friedman 2001](#)), to mitigate high variance and overfitting, which can be serious when the signal-to-noise ratio is low. Wavelet transforms and ensembles thus present two complementary approaches for reducing variance. A natural question is whether incorporating both approaches simultaneously in a single framework can lead to further improvements in the resulting estimation and inference.

Following this motivation, we introduce an additive boosted ensemble model of weak wavelet-based tree learners. Whereas standard boosted regression trees regularize only at the leaf-level of the partition trees, each of our weak learners is a strongly regularized estimator along a binary recursive partition tree over the function domain, with regularization enforced under a wavelet basis along the partition tree. Standard wavelet transforms, however, are defined on dyadic trees that partition at fixed midpoints of the domain dimensions, which limits the diversity of the collection of trees and hence leads to large bias or approximation error in the resulting additive ensemble. To overcome this limitation, we employ an “unbalanced” Haar wavelet transform defined on partition trees that can be divided into a rich set of possible locations. Ensemble ideas for wavelet-based generative models also appear in [Xie et al. \(2016\)](#), who introduce wavelets into a boosting framework and incrementally build complex models for wavelet coefficients.

We carry out a theoretical analysis to understand the difference in asymptotic behaviors of standard regression trees such as CART, which we refer to as leafwise estimators, and

wavelet-based regression trees with unbalanced bases, which estimate coefficients and impose regularization on interior nodes of the partition tree. We derive oracle bounds showing that the stochastic term for the UH estimator scales with the number of active coefficients, while the corresponding term for the leafwise estimator scales with the total number of leaves. This clarifies when reconstruction based on UH coefficients can substantially reduce variance, particularly for signals that are sparse in the corresponding dictionary.

In addition, we construct a new regression framework based on orthogonal unbalanced Haar (UH) wavelet trees (UHWT) whose main target is regression on triangulable manifolds. The framework further connects classical wavelet and tree methodology and extends additive ensembles to non-Euclidean domains, while reducing to standard UHWT regression on regular Euclidean grids as a special case. To this end, we extend UHWT from two-dimensional images to higher-order tensors and triangulable manifold domains. On the latter, we work with geodesic triangulations and data-adaptive recursive splits of triangles, which yield an orthonormal unbalanced Haar system in  $L^2(\mu_n)$  on curved domains. This construction permits a data-driven wavelet regression ensemble for generic non-Euclidean spaces. We use UH trees as weak learners in additive ensembles and employ random rigid motions, for example, rotations on the sphere or intrinsic reparameterizations, to generate diverse trees while preserving the geometry of the domain. This unbalanced construction has concrete advantages over more rigid multiresolution schemes, such as balanced Haar bases on fixed spherical grids or fixed-depth trees. Balanced constructions split every cell according to a predetermined schedule, regardless of the data, and they typically rely on global coordinate systems that distort geometry on curved surfaces. In contrast, UH trees choose split locations along edges using the empirical masses and local variation of the data, so partitions can be simultaneously highly refined near sharp transitions on the manifold and coarse in smooth or low-data regions. This adaptivity is particularly important when triangle shapes and sampling densities vary across the surface, as in our spherical examples.

While we mainly take an optimization approach to risk minimization in designing our algorithms for fitting our estimators, for completeness, we also present a probabilistic formulation of the unbalanced wavelet-tree ensemble model, where a prior distribution over split dimensions and locations induces a prior distribution over UH trees, and a wavelet likelihood factor leads to a posterior distribution over tree structures with direct uncertainty quantification for shapes (Luo & Strait 2024). The latter formulation leads to a Bayesian backfitting algorithm that parallels that for fitting Bayesian Additive Regression Trees (BART) (Chipman et al. 2010).

To our knowledge, this is the first framework that combines orthogonal wavelets, recursive partitions that are aware of manifold geometry, and modern ensemble techniques into a unified regression method on triangulable manifolds. The remainder of the paper develops UHWTs on grids and triangulated manifolds (Sections 2–3), their optimization-based and Bayesian ensembles (Section 4). Section 5 investigates the theoretical properties of our methods. Section 6 presents empirical evaluations using diverse real and synthetic datasets.

## 2 Wavelet Tree Regression

Signal denoising is a fundamental task in signal processing and can be formulated as a regression problem. For a domain  $\Omega$ , we aim to recover a signal  $f: \Omega \rightarrow \mathbb{R}$  from observations

$$y_i = f(\mathbf{x}_i) + \epsilon_i, \quad i = 1, \dots, n \quad (1)$$

at locations  $\mathbf{x}_i \in \Omega$  with zero mean additive noise  $\epsilon_i$  that is stable under orthogonal wavelet transforms. Classical wavelet denoising proceeds by projecting the noisy signal onto a wavelet system (Mallat 1999), shrinking the resulting coefficients, and reconstructing a smoothed version of the signal (Donoho et al. 1995). In this section, we construct a wavelet representation along a binary tree that links directly to regression trees and lays the groundwork for both the optimization and Bayesian approaches developed later. These two approaches share the same Haar representation and the same notion of wavelet coefficients attached to nodes of a tree, but they differ in how splits are chosen and how regularization is imposed. The remainder of Section 2 will assume that the domain  $\Omega \subset [0, 1]^D$  is a known, regular grid  $\{1/n_1, \dots, 1\} \times \{1/n_2, \dots, 1\} \times \dots \times \{1/n_D, \dots, 1\}$  for some  $D \in \mathbb{N}$ , where usually  $D = 2$  (e.g., an image) or  $D = 3$  (e.g., a video or a spatial temporal field). Section 3 will then introduce our methodology for when  $\Omega$  is a triangulable manifold (e.g., a sphere). For simplicity, the entire paper will assume that the locations  $\mathbf{x}_1, \dots, \mathbf{x}_n$  are unique.

### 2.1 Unbalanced Haar Wavelet Tree

The choice of wavelet functions determines how well the procedure captures the structure of the data. To realize the potential of ensembling over wavelet regression as base learners, we need to enable enough diversity among the partition trees. As such, we must depart from standard wavelets that always partition in a balanced fashion at the midpoints of the domain dimensions, and consider unbalanced domain partitions. While in general this strategy can be incorporated for any wavelet basis, the Haar basis enjoys computational simplicity (Li & Ma 2021). Thus we start by constructing unbalanced Haar (UH) functions through a recursive binary partitioning of the grid domain  $\Omega$ .

Starting with  $A = \Omega$ , we select—either greedily or probabilistically—a “valid” dimension  $d \in \{1, \dots, D\}$  and then select a “valid” location  $\ell \in (a, b)$ , where  $a$  and  $b$  are the endpoints of the marginal interval of  $A$  along dimension  $d$ . We call a dimension/location *valid* if the node can be bisected along that dimension/location. The set  $A$  is then bisected along dimension  $d$  at location  $\ell$  into two disjoint pieces,  $A_l$  and  $A_r$ .

For this split  $(A, d, \ell)$ , we define the UH wavelet function by

$$\psi_{A,d,\ell}(\mathbf{x}) = \sqrt{\frac{|A_l| |A_r|}{|A|}} \left( \frac{\mathbf{1}\{\mathbf{x} \in A_l\}}{|A_l|} - \frac{\mathbf{1}\{\mathbf{x} \in A_r\}}{|A_r|} \right), \quad (2)$$

where  $|\cdot|$  denotes the  $\mu$ -measure of a set for a fixed base measure  $\mu$  on  $\Omega$  (e.g., Lebesgue measure in the classical setting or the empirical measure  $\mu_n$  in our finite-sample theory).

In classical wavelet regression (Mallat 1989), one chooses a *pre-defined* family of wavelets. In a data-driven regression tree, the same splitting construction is applied recursively to

each piece,  $A_l$  and  $A_r$ , that can be split. In this way, a recursive partition and a family of UH functions (2) are built in parallel. The collection of functions generated in this way forms a dictionary of piecewise-constant functions supported on sets of varying shapes and locations (Friedman & Tukey 1974, Donoho 1997). This dictionary is not necessarily a complete basis of  $L^2([0, 1]^D)$ , but it is sufficiently rich for regression on the observed design.

Given such a recursive binary partition, each split  $(A, d, \ell)$  can be associated with an internal node of a binary tree rooted at  $\Omega$ ; we will call it an *Unbalanced Haar Wavelet Tree* (UHWT). Each split is also associated with a wavelet coefficient defined as the  $L^2(\mu)$  inner product

$$w_{d,\ell}(A) := \langle \psi_{A,d,\ell}, y \rangle_{L^2(\mu)} = \sqrt{\frac{|A_l^{(d,\ell)}| |A_r^{(d,\ell)}|}{|A|}} \left( \frac{\int_{A_l^{(d,\ell)}} y(\mathbf{x}) d\mu(\mathbf{x})}{|A_l^{(d,\ell)}|} - \frac{\int_{A_r^{(d,\ell)}} y(\mathbf{x}) d\mu(\mathbf{x})}{|A_r^{(d,\ell)}|} \right) \quad (3)$$

where  $A_l^{(d,\ell)}$  and  $A_r^{(d,\ell)}$  denote the left and right children obtained by splitting  $A$  at  $(d, \ell)$ . When the domain  $\Omega$  is a regular grid and we take  $\mu$  to be the empirical measure  $\mu_n = n^{-1} \sum_{i=1}^n \delta_{\mathbf{x}_i}$ , for any node  $A$  we have  $\int_A y(\mathbf{x}) d\mu_n(\mathbf{x}) = n_A^{-1} \sum_{\mathbf{x}_i \in A} y_i$  and  $\mu_n(A) = n_A/n$ , where  $n_A$  is the number of design points in  $A$ . Substituting into (3) implies  $w_{d,\ell}(A) = \sqrt{\frac{n_l n_r}{n_A}} (\bar{y}_l - \bar{y}_r)$ , where  $\bar{y}_B = n_B^{-1} \sum_{\mathbf{x}_i \in B} y_i$  denotes the sample mean in node  $B$ . The observed signal can then be reconstructed using an empirical inverse transform. Denoising the signal, however, will require regularizing the coefficients, as will be discussed in Section 2.2.

Related connections between Haar wavelets and regression trees include Donoho (1997) and Fryzlewicz (2007). Our construction allows continuous split locations in multiple dimensions, and in the grid case the inverse UH transform coincides exactly with the leafwise CART estimator on the same tree (online Appendix C; see also online Appendix G.3).

Our construction allows continuous split locations in multiple dimensions and, in the grid case, we show in online Appendix C that the associated regression fit coincides exactly with the leafwise CART estimator on the same tree (see online Appendix G.3 for a connection to Fryzlewicz (2007)).

As will be shown below, our UH construction is algebraically agnostic and can be extended to accommodate tensors; In contrast, the tensor-tree method of Luo et al. (2025) is explicitly tensor aware: it evaluates splits using low-rank approximation errors, for example based on CP or Tucker reconstructions, and fits low-rank models inside leaves. Our UHWT tensor method instead emphasizes geometric splits and Haar contrasts and is designed for signals with local discontinuities or anisotropic edges.

## 2.2 The optimization approach to fitting a UHWT

In the optimization approach, each split in the UHWT is chosen greedily and deterministically from the data. (Online Appendix C explores the connection of our method to CART in the grid case.) At each node  $A$ , this approach chooses a split dimension and location pair  $(d, \ell)$  that maximizes the absolute value of the coefficient  $w_{d,\ell}(A)$  from (3),

$$(d^*, \ell^*) \in \arg \max_{(d,\ell)} |w_{d,\ell}(A)|, \quad (4)$$

subject to basic safeguards such as minimum sample sizes in the children, as described in online Appendix A, and optional stopping rules. Because the UH scaling and wavelet

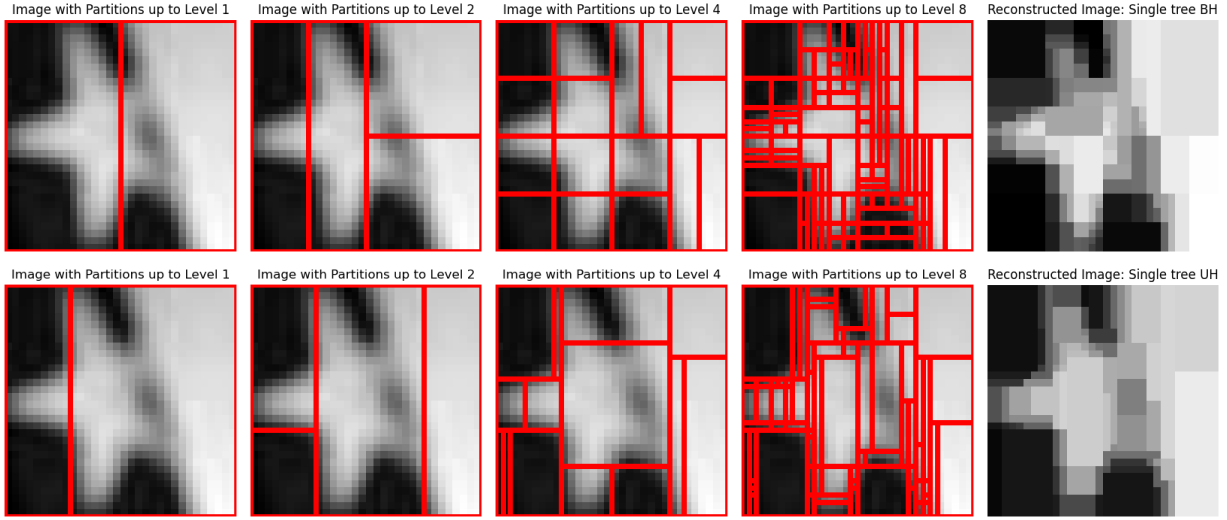


Figure 1: Comparison between the Balanced Haar (BH) and UH optimization approach on a noisy image that contains a star and a mostly two tone background. The first row uses BH splits. The second row uses UH splits chosen by optimization; these splits delineate the boundary of the star and adapt to the volume of the main object. At depth 8 the partitions concentrate along the edges of the star. The final reconstruction with a single tree preserves both the boundary and the volume of the star while reducing background interference.

functions form an orthonormal system in  $L^2(\mu_n)$  (see Section 5 and online Appendix B), the immediate reduction in empirical squared error achieved by splitting at  $(d, \ell)$  is exactly  $|w_{d,\ell}(A)|^2$ . Thus the criterion (4) selects the split with the largest one-step reduction in empirical risk on node  $A$ .

Each greedy split (4) requires the computation of wavelet coefficients for many possible splits. To reduce the amount of computation, we will use an early stopping mechanism: if the wavelet coefficient for an internal node  $A$  falls below the threshold  $b\hat{\sigma}$  for  $\hat{\sigma}$  defined in (6) and some user-chosen constant  $b \geq 0$ , then  $A$  will be set to a leaf node that is no longer allowed to split. This is optional if we ultimately fit just a single tree, but it will prove to be computationally crucial when we construct ensembles of wavelet trees as in Section 4. Figure 2 in online Appendix L.1.2 provides empirical results on an image dataset for using both the soft-thresholding and early-stopping mechanisms.

After the binary partition tree is generated, a denoised signal is obtained by an empirical inverse transform on the learned binary-tree partition  $\mathcal{P}_n$  using possibly regularized versions of the wavelet coefficients. The transform at any location  $\mathbf{x}$  is described as follows. Let  $A_0 \supset A_1 \supset \dots \supset A_{S(\mathbf{x})}$  be the sequence of nodes along the path from the root  $A_0$  to the leaf  $A_{S(\mathbf{x})}$  containing  $\mathbf{x}$ . For each internal node  $A_i$  on this path  $1, 2, \dots, S(\mathbf{x})$ , we store the coefficient  $w_{d_i, \ell_i}(A_i)$ . For some regularized versions of these coefficients, which we will denote as  $\tilde{w}_{d_i, \ell_i}(A_i)$ , we define the denoised signal

$$\hat{f}_{\mathcal{P}_n}^{\text{UH}}(\mathbf{x}) = \frac{1}{n} \sum_{i=1}^n y_i + \sum_{i=0}^{S(\mathbf{x})-1} u_i \frac{\tilde{w}_{d_i, \ell(A_i)}(A_i)}{c(A_i)}, \quad c(A_i) = |A_i|^{1/2} \left( \frac{|A_{i,l}^{(d_i)}|}{|A_{i,r}^{(d_i)}|} \right)^{u_i/2}, \quad (5)$$

where  $u_i = 1$  if  $\mathbf{x}$  is in the left child of  $A_i$  and  $u_i = -1$  if  $\mathbf{x}$  is in the right child. The

normalization  $c(A_i)$  corresponds to the UH normalization and ensures orthonormality in  $L^2(\mu_n)$ . If  $\tilde{w}_{d,\ell}(A) = w_{d,\ell}(A)$  for all splits in  $\mathcal{P}_n$ , and if the leaves of  $\mathcal{P}_n$  each contain exactly one training location, then the original observed (noisy) signal is recovered.

The amount and quality of denoising will depend on the early stopping and how the wavelet coefficients are regularized in (5). Our optimization approach will involve two main ingredients. The first ingredient is an estimate of the noise level based on a robust scale measure. Let  $\mathcal{W}_{\text{deep}}$  denote a collection of coefficients at deep levels of the tree where the signal is expected to be weak. We define

$$\hat{\sigma} = \frac{\text{MAD}\{w_{d,\ell}(A) : (A, d, \ell) \in \mathcal{W}_{\text{deep}}\}}{0.6745}, \quad (6)$$

where MAD is the median absolute deviation recommended by [Nason \(2008\)](#). This estimator is widely used in wavelet denoising and is stable in the presence of a small number of large coefficients (See Sec 5). The second ingredient is a separate threshold applied at reconstruction. Once the tree is grown and the coefficients  $w_{d,\ell}(A)$  are stored at each internal node, we compute soft-thresholded coefficients

$$\tilde{w}_{d,\ell}(A) = \text{sign}(w_{d,\ell}(A)) \left( |w_{d,\ell}(A)| - \tau \right)_+, \quad (7)$$

with threshold  $\tau = a \hat{\sigma} \sqrt{2 \log n}$  for some user-chosen constant  $a \geq 0$ . More sophisticated ways of thresholding can be used; we will leave this exploration for future work.

## 2.3 Bayesian modeling and sampling on UHWTs

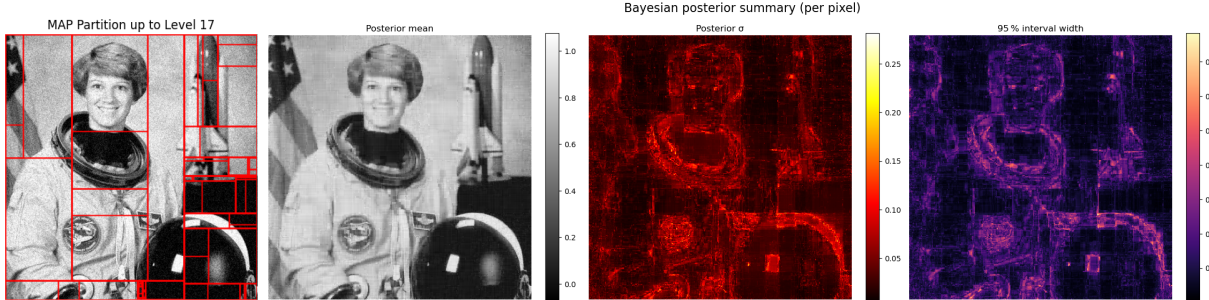


Figure 2: First panel: MAP partition overlaid on the input image. Posterior mean (second panel), standard deviation (third panel), and 95% credible interval width (fourth panel) computed from 500 full posterior draws of a Bayesian additive UH-tree model with 200 trees and geometric early-stopping prior probability  $0.5^{\text{node depth}}$ .

The optimization approach will produce a point estimate for the underlying signal function without any associated uncertainty. In contrast, a Bayesian modeling and sampling approach will induce stochastic sampling from the corresponding posterior distribution, directly allowing uncertainty quantification as shown in Figure 2. The prerequisite is to specify a prior distribution on the space of UHWTs. Earlier literature introduced a number of priors for wavelets defined on fixed trees splitted at mid-points ([Li & Ma 2021](#)). Here we allow unbalanced splits, which will be critical for our later ensembling.

Here we describe our prior, which we call a random UHWT (RUHWT) model. We start at the root node  $A_0 = \{\Omega\}$ . For any node  $A$  that can be split, we draw a split dimension  $D(A)$  from a set  $\mathcal{D}(A)$  of admissible split dimensions according to probability mass function  $\{\lambda_d(A): d \in \mathcal{D}(A)\}$  and then draw a split location  $L(A)$  from a distribution  $B_{A,d}$  on the unit interval. The following theorems will allow  $B_{A,d}$  to have full support on  $[0, 1]$ , but for a grid-domain application, each  $B_{A,d}$  is a discrete distribution on the set  $\{i/n_A: i = 1, \dots, (n_A-1)\}$ ; we could then specify median splits by setting each  $B_{A,d}$  to be a point mass at 0.5 (assuming  $n_A$  is divisible by two).

Given a tree  $T$  and its UH system, we specify a Bayesian wavelet model. In the simplest case, we assume that the UH coefficients are independent and identically distributed under a parametric family  $p_i(w, z | \phi)$  — see (8) — where  $z$  are local latent variables and  $\phi$  are hyperparameters. The following theorem expresses the marginal posterior for  $T$  in terms of updated split probabilities that combine the prior weights  $\lambda_d(A)$ ,  $B_{A,d}$  and local marginal likelihoods based on the same coefficients  $w_{d,\ell}(A)$  that drive the optimization rule.

**Theorem 2.1.** *Suppose  $T$  has a RUHWT prior with split dimension probabilities  $\{\lambda_d(A): A \in \mathcal{A}, d \in \mathcal{D}(A)\}$  and split location distributions  $\{B_{A,d}: A \in \mathcal{A}, d \in \mathcal{D}(A)\}$  on  $[0, 1]$ , with zero probability of creating a child with no training locations. Suppose that, given  $T$  and hyperparameters  $\phi$ , the wavelet coefficients satisfy*

$$(w_i, z_i) \stackrel{\text{ind}}{\sim} p_i(w, z | \phi), \quad \text{for all } A_i \in T. \quad (8)$$

*Then the marginal posterior of  $T$  is a RUHWT with posterior splitting probabilities*

$$P(D(A) = d | \mathbf{y}) \propto \lambda_d(A) \int_0^1 M_{d,\ell}(A) \Phi(A_l^{(d,\ell)}) \Phi(A_r^{(d,\ell)}) dB_{A,d}(\ell), \quad (9)$$

*and conditional split location distribution*

$$dB_{A,d}(\ell | D(A) = d, \mathbf{y}) \propto dB_{A,d}(\ell) M_{d,\ell}(A) \Phi(A_l^{(d,\ell)}) \Phi(A_r^{(d,\ell)}), \quad (10)$$

*where  $M_{d,\ell}(A_i) = \int p_i(w_{d,\ell}(A_i), z | \phi) dz$  is the marginal likelihood contribution of the coefficient at node  $A_i$  if it is split at  $(d, \ell)$ , and  $\Phi(A)$  satisfies*

$$\Phi(A) = \sum_{d \in \mathcal{D}(A)} \lambda_d(A) \int_0^1 M_{d,\ell}(A) \Phi(A_l^{(d,\ell)}) \Phi(A_r^{(d,\ell)}) dB_{A,d}(\ell) \quad (11)$$

*when  $A$  is not atomic and  $\Phi(A) = 1$  when  $A$  is atomic.*

Theorem 2.1 provides a posterior distribution on the space of axis-aligned, binary-tree partitions; such a partition will establish a one-to-one correspondence between the leaves of the tree and the training locations  $\{\mathbf{x}_i\}$  if the prior distributions on the splitting dimensions and locations are positive for admissible split dimensions and locations. A signal can then be constructed from the partition's associated UH coefficients, but if the coefficients are not regularized, then the constructed signal will be exactly the original observed signal. We can denoise the signal by introducing latent state variables at each node that, for example, determine whether the node will be split or how the resulting wavelet coefficient will contribute to the reconstructed signal (this is analogous to our optimization approach's splitting safeguards, early stopping mechanism, and soft thresholding). Theorem E.1 (stated

and explained in online Appendix E for space reasons) extends Theorem 2.1 to incorporate latent states.

Theorems 2.1 and E.1 generalize recursive partition posteriors in Li & Ma (2021) by allowing data-driven split locations and UH systems on irregular designs. The same coefficients  $w_{d,\ell}(A)$  that determine the greedy optimization rule now enter through the marginal likelihood factors  $M_{d,\ell}(A)$  and guide the posterior choice of splits. In the optimization framework, regularization is applied through MAD-based thresholds applied to coefficients on a fixed tree. In the Bayesian framework, regularization is applied through depth-dependent split probabilities and the latent states.

When the prior on splits is diffuse and the likelihood is sharply peaked at the largest  $|w_{d,\ell}(A)|$  (we provide spike-and-slab and Laplace priors in implementation), the posterior split probabilities concentrate near the maximizing pair of the optimization rule, so the greedy algorithm appears as a limiting case. This parallel viewpoint will be important when we construct ensembles and extend the methods to triangulable manifolds in later sections.

### 3 Wavelet Trees for Triangulable Manifold Domains

We now describe our second major step in generalizing UHWTs. The goal is to define wavelet trees on spheres or more general triangulable manifolds while retaining the key features of the Euclidean construction: orthogonality in  $L^2(\mu_n)$ , exact reconstruction at the sampled locations, and the ability to support both optimization-based and Bayesian tree building. These properties are crucial for the ensemble methods on manifolds that will be developed in later sections.

A curved surface has no coordinate axes that provide natural directions along which to split. Our approach thus rests on the fact that any compact orientable two-dimensional manifold can be approximated, and in fact partitioned, by a finite simplicial complex of geodesic triangles, which exists on a *triangulable manifold* (Edelsbrunner & Shah 1994). In most practical scenarios, the manifold of interest is triangulable. We therefore assume that the domain  $\mathcal{M}$  is a compact orientable two-dimensional manifold endowed with an area measure  $\mathcal{H}^2$ , and that we are given an initial triangulation whose faces are geodesic triangles. On the sphere, we take the initial triangulation to be a geodesic polyhedron, such as the icosahedron (Schröder & Sweldens 1995); on a generic surface, we use any admissible simplicial complex. The same ideas apply to *any manifold* that admits such a triangulation.

A geodesic triangle can be bisected by connecting a point  $\xi$  on an edge  $e \in \{1, 2, \dots, D\}$  to the opposite vertex via a geodesic arc. This split's UH coefficient is defined by

$$w(A, e, \xi) = \sqrt{\frac{\mu_n(A_1) \mu_n(A_2)}{\mu_n(A)}} (\bar{y}_{A_1} - \bar{y}_{A_2}), \quad \bar{y}_{A_j} = \frac{1}{\mu_n(A_j)} \int_{A_j} y \, d\mu_n, \quad (12)$$

where  $A_1$  and  $A_2$  are the two child triangles that result from the split, and  $\mu_n = n^{-1} \sum_{i=1}^n \delta_{\mathbf{x}_i}$  is the empirical measure of the observed locations  $\mathbf{x}_1, \dots, \mathbf{x}_n \in \mathcal{M}$ . The associated UH wavelet function  $\psi_{A,e,\xi}$  is defined as in (2) with  $|B|$  interpreted as  $\mu_n(B)$ . With this choice, the UH scaling and wavelet functions form an orthonormal system in  $L^2(\mu_n)$  on the triangulated manifold, exactly as in the rectangular case. We still use the geometric

area  $|A| = \int_A d\mathcal{H}^2$  to control triangle shape regularity and to specify admissible splits, but orthonormality is always defined with respect to  $\mu_n$ . Thus each triple  $(A, e, \xi)$  defines a UH atom on the manifold in exactly the same way that  $(A, d, \ell)$  defines a UH atom in the Euclidean setting. For visualization, we discuss  $D = 3$  hereafter, but emphasize that our construction works for any  $D \in \mathbb{N}$ .

Compared to a balanced Haar construction on a fixed spherical grid, this edge-cut representation together with the unbalanced normalization have two advantages on manifolds. First, the split point  $\xi$  can move freely along an edge, so triangles can be cut in a strongly unbalanced way when the response varies sharply along a boundary while remaining intact when the response is nearly constant. Second, because the normalization is defined with respect to  $\mu_n$ , the associated wavelet atoms still form an orthonormal system in  $L^2(\mu_n)$ , so each coefficient  $w(A, e, \xi)$  measures the empirical energy of the contrast between the two child triangles. In practice, this leads each UH tree to concentrate depth where the regression function exhibits localized structure on the manifold and, when aggregated in an ensemble, to yield sparse representations and improved predictive performance on the spherical regression problems in Section 6.

The optimization and Bayesian tree building rules extend to this setting. In the optimization approach, at a node  $A$  we choose the admissible edge-cut pair  $(e, \xi)$  that maximizes  $|w(A, e, \xi)|$ . Splitting along  $(e, \xi)$  decreases empirical squared error by  $|w(A, e, \xi)|^2$ , so the greedy rule has the same interpretation as in the rectangular case. In the Bayesian approach, the RUHWT prior can now be defined on sequences of edge-cut pairs  $(e, \xi)$ , with  $\lambda_e(A)$  and  $B_{A,e}$  replacing  $\lambda_d(A)$  and  $B_{A,d}$  in Theorems 2.1 and E.1. The same coefficients  $w(A, e, \xi)$  enter the marginal likelihood factors  $M_{A,e,\xi}$ , so the optimization and Bayesian constructions share the same empirical contrasts.

Figure 3 shows four splitting rules for triangles. The rule called **balance** is a classical mid-edge bisection: the longest edge of the parent triangle is bisected at its geodesic midpoint, and the far vertex is joined to this midpoint by a geodesic segment. The rule called **adapt** is also a mid-edge bisection, but it chooses the edge whose geodesic midpoint produces the largest magnitude UH coefficient among all three edges. The rule called **adapt\_vertex** is fully point adaptive. Each interior data point in  $A$  is projected orthogonally onto each edge, and the pair consisting of an edge and a projection point that maximizes  $|w(A, e, \xi)|$  is selected; the geodesic segment connecting this projection point to the opposite vertex defines the two children. The rule called **balance4** is a canonical four-child split that connects the three edge midpoints to form four triangles inside  $A$  (Schröder & Sweldens 1995). The **adapt** and **adapt\_vertex** rules favor anisotropic adaptation; repeated splits refine precisely those edges where the empirical function varies most, while nearby regions with little variation remain coarse. The **balance** and **balance4** rules favor shape regularity. In all cases, after the tree is grown we apply the same reconstruction-time thresholding of UH coefficients described in (12), with thresholds calibrated from a MAD estimate of noise on fine scale coefficients. This keeps the partition from reflecting noise or irregular sampling artifacts and ensures that deep refinements correspond to genuine local variation.

Table 1 in online Appendix J summarizes the asymptotic training complexity for these four splitting rules (online Appendix L.3.2 has an empirical comparison). The main computational cost arises from determining which sample points lie in each child triangle.

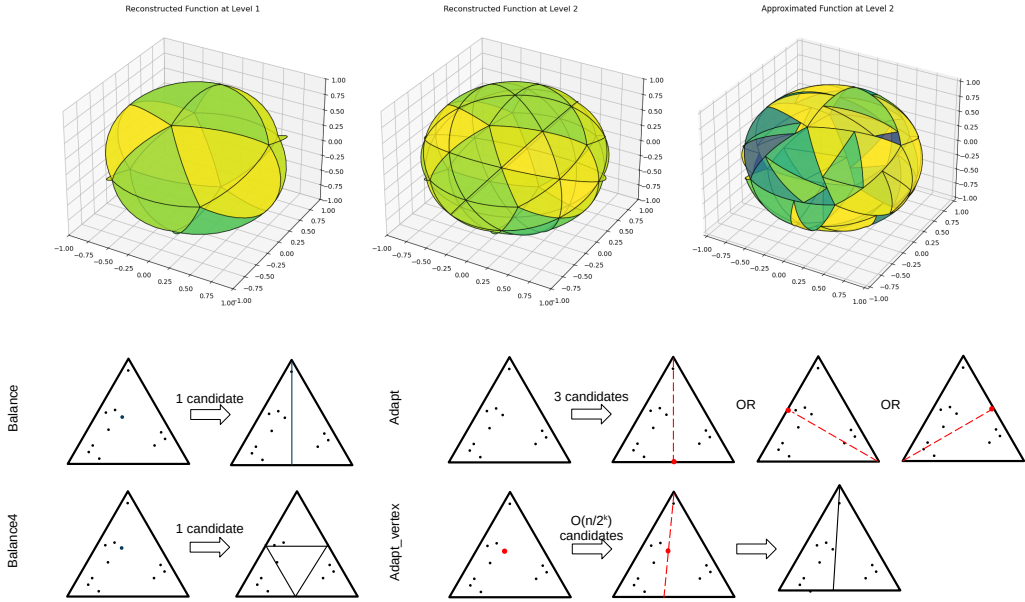


Figure 3: Examples of triangulable manifolds and four approaches (`balance`, `balance4`, `adapt`, `adapt_vertex`) to subdivide a triangle. Points represent data; the red point indicates the pivot point, and dashed lines show the cutting edge. The `balance` and `balance4` schemes do not depend on data. The `adapt` scheme uses data to choose which edge to bisect at its midpoint. The `adapt_vertex` scheme uses data to choose both the edge and the cut point.

A triangulation and barycentric membership test suffice for this.

To summarize, the triangulable manifold constructions extend classical tree methods to more general domains, and also extend the UH tree framework from (hyper)rectangular grid data to triangulable manifolds. Both the optimization and Bayesian constructions extend naturally: in each case the same UH coefficients guide split selection, and regularization is imposed either by MAD-based thresholding at reconstruction or by biased priors and posterior shrinkage in the RUHWT model. (Online Appendix K compares our UHWT model on a triangulable manifold to other existing tree-based methods for manifold domains.) These constructions will form the basis for the ensemble methods developed in the next section.

## 4 Additive Unbalanced Haar Wavelet Tree Ensembles

Ensembles improve prediction by combining many weak learners. Random Forests typically grow deep trees, which can be less compatible with sparse multiscale representations. In contrast, classical boosting and BART regularize by restricting the number of leaf nodes in each tree. Unlike tree fits used in previous methods, UHWTs provide orthogonal expansions with wavelet coefficient-based shrinkage. We thus aim to construct both a boosting algorithm and a Bayesian method analogous to BART, using the UHWT as the weak learner.

A single UH tree  $T$  yields the orthogonal expansion

$$g(\mathbf{x}) = \bar{y}_\Omega + \sum_{j \in J(T)} \tilde{w}_j \psi_j(\mathbf{x}). \quad (13)$$

Here  $\bar{y}_\Omega := n^{-1} \sum_{i=1}^n y_i$  is the global mean;  $\mathcal{P}(T)$  denotes the recursive partition induced by  $T$ ;  $J(T)$  indexes the internal nodes/splits of  $T$  and hence the non-constant UH atoms;  $\{\psi_j\}_{j \in J(T)}$  are those UH atoms, normalized to be orthonormal in  $L^2(\mu_n)$  as in Section 2.2; and  $\tilde{w}_j$  are (possibly shrunk) empirical coefficients.

## 4.1 Boosting for UHWTs

In general, forward stagewise boosting (Friedman 2001) builds an ensemble model  $f_G(\cdot)$ ,  $G \in \mathbb{N}$  by iteratively adding “weak” learners  $g_t(\cdot)$ ,  $t = 1, \dots, G$  to improve predictions. Our weak learners will belong to the class  $\mathcal{G}$  of UH tree fits built by the optimization approach of Section 2.2 (using the UH coefficients (3) and the greedy split rule (4)). The fits are then further regularized by a pre-chosen learning rate  $\eta \in (0, 1]$ . Hence, our procedure is forward stagewise boosting specialized to UH trees; the difference from CART-based boosting is that each  $g_t$  comes with an orthonormal UH expansion and admits coefficient shrinkage.

Let  $\{(\mathbf{x}_i, y_i)\}_{i=1}^n$  be training data on  $\Omega$  with empirical measure  $\mu_n$ , and let  $y$  denote the observed signal viewed as a function on the sample. We use the squared-error loss  $\frac{1}{2n} \sum_{i=1}^n (y_i - f(\mathbf{x}_i))^2 = \frac{1}{2} \|y - f\|_{L^2(\mu_n)}^2$  and initialize  $f_0(\mathbf{x}) \equiv \bar{y}_\Omega$ . At each stage  $t = 1, \dots, G$ , our ensemble model  $f_t$  will be updated as

$$f_t(\mathbf{x}) = f_{t-1}(\mathbf{x}) + \eta g_t(\mathbf{x}), \quad (14)$$

where the weak learner  $g_t \in \mathcal{G}$  is fit to residuals  $r_{t-1,i} := y_i - f_{t-1}(\mathbf{x}_i)$ ,  $i = 1, \dots, n$ , by (approximately) solving

$$g_t \in \arg \min_{g \in \mathcal{G}} \frac{1}{2n} \sum_{i=1}^n (r_{t-1,i} - g(\mathbf{x}_i))^2. \quad (15)$$

A UHWT weak learner built on the residuals has the form

$$g_t(\mathbf{x}) = \sum_{j \in J(T_t)} \tilde{c}_j^{(t)} \psi_j^{(t)}(\mathbf{x}), \quad \tilde{c}_j^{(t)} = \text{sign}\left(c_j^{(t)}\right) \left(\left|c_j^{(t)}\right| - \tau_t\right)_+, \quad c_j^{(t)} = \langle r_{t-1}, \psi_j^{(t)} \rangle_{L^2(\mu_n)}. \quad (16)$$

Here  $T_t$  is the fitted UH tree at stage  $t$ ;  $J(T_t)$  indexes its internal nodes/splits;  $\psi_j^{(t)}$  are the corresponding UH atoms (orthonormal in  $L^2(\mu_n)$ );  $\langle \cdot, \cdot \rangle_{L^2(\mu_n)}$  is the empirical inner product; and  $(u)_+ := \max\{u, 0\}$ . The threshold  $\tau_t$  is calibrated from a MAD estimate of noise on fine-scale residual coefficients (as in Section 2.2).

To connect (15) to UH orthogonality, fix a candidate tree  $T$  and write  $g$  supported on  $T$  as  $g(\mathbf{x}) = \sum_{j \in J(T)} \theta_j \psi_j(\mathbf{x})$ . Substituting this into (15), orthonormality in  $L^2(\mu_n)$  yields

$$\frac{1}{2} \|r_{t-1} - g\|_{L^2(\mu_n)}^2 = \frac{1}{2} \|r_{t-1}\|_{L^2(\mu_n)}^2 - \sum_{j \in J(T)} \theta_j \langle r_{t-1}, \psi_j \rangle_{L^2(\mu_n)} + \frac{1}{2} \sum_{j \in J(T)} \theta_j^2. \quad (17)$$

For fixed  $T$ , the minimizer over  $\theta$  is  $\theta_j^* = \langle r_{t-1}, \psi_j \rangle_{L^2(\mu_n)}$  for all  $j \in J(T)$ , and the associated risk reduction has the same form as in orthogonal wavelet shrinkage (Donoho et al. 1995).

Using the UHWT fitting (See online Appendix G.4), on the sphere we draw  $R_t \in \text{SO}(3)$  from Haar measure and build  $T_t$  (hence  $\psi_j^{(t)}$ ) on the rotated locations  $R_t \mathbf{x}_i$ . The residuals  $r_{t-1,i}$  remain evaluated at  $\mathbf{x}_i$ , but the learner is pulled back by composition:

$$g_t(\mathbf{x}) = \sum_{j \in J(T_t)} \tilde{c}_j^{(t)} \psi_j^{(t)}(R_t \mathbf{x}), \quad f_t(\mathbf{x}) = f_{t-1}(\mathbf{x}) + \eta g_t(\mathbf{x}). \quad (18)$$

On a general triangulable manifold  $\mathcal{M}$ , we replace  $R_t$  in (18) by a random intrinsic reparameterization  $\Phi_t$ . On spheres, we provide two options: Euclidean PCA and sPCA (Luo et al. 2024), as shown later in Section 6.

## 4.2 Bayesian backfitting sampling for RUHWT ensembles

We now describe a Bayesian ensemble that builds on the RUHWT model of Section 2.3 and uses Bayesian backfitting (Hastie & Tibshirani 2000, Chipman et al. 2010). Let  $m$  denote the number of component trees in the ensemble. We model

$$f_m(\mathbf{x}) = \mu + \sum_{t=1}^m g_t(\mathbf{x}; \theta_t), \quad (19)$$

where  $\mu$  is a global intercept and each  $\theta_t$  collects the  $t$ th tree structure, its UH coefficients, and any local scales under the RUHWT prior. Conditional on  $f_m$ ,

$$y_i = f_m(\mathbf{x}_i) + \epsilon_i, \quad \epsilon_i \sim N(0, \sigma^2), \quad i = 1, \dots, n. \quad (20)$$

We place a prior  $p(\mu, \sigma^2)$  on global parameters and independent RUHWT priors on  $\theta_1, \dots, \theta_m$  as in Section 2.3. A Gibbs sampler cycles through components and conditionally updates  $\theta_t$  given the others by fitting a RUHWT to the current partial residual.

Given a pre-defined number of sweeps, at component  $t \in \{1, \dots, m\}$  and sweep  $s$  we define

$$r_{t,i}^{(s)} = y_i - \mu^{(s)} - \sum_{k \neq t} g_k(\mathbf{x}_i; \theta_k^{(s)}), \quad i = 1, \dots, n, \quad (21)$$

and update  $\theta_t$  from its conditional posterior

$$p(\theta_t | r_t^{(s)}, \sigma^2) \propto p(\theta_t) \prod_{i=1}^n \exp \left\{ -\frac{1}{2\sigma^2} (r_{t,i}^{(s)} - g_t(\mathbf{x}_i; \theta_t))^2 \right\}. \quad (22)$$

We use Metropolis-within-Gibbs proposals that locally modify  $\theta_t$  and accept/reject via the usual Metropolis ratio. (The “latent-state Markov tree” regularization referenced in Theorem E.1 in online Appendix E is the same as in Section 2.3 and is distinct from the UH trees  $T_t$ .)

Orthogonality yields simple coefficient updates in a fixed tree. For example, if the coefficient on atom  $\psi_j^{(t)}$  has prior  $w_j^{(t)} \sim N(0, \tau_t^2)$ , then under (20) its conditional posterior satisfies

$$\text{Var}(w_j^{(t)} | T_t, r_t^{(s)}, \sigma^2) = \left( \frac{1}{\tau_t^2} + \frac{1}{\sigma^2} \right)^{-1}, \quad (23)$$

$$\mathbb{E}[w_j^{(t)} | T_t, r_t^{(s)}, \sigma^2] = \text{Var}(w_j^{(t)} | T_t, r_t^{(s)}, \sigma^2) \frac{\langle r_t^{(s)}, \psi_j^{(t)} \rangle_{L^2(\mu_n)}}{\sigma^2}. \quad (24)$$

More flexible priors (e.g., spike-and-slab or global-local shrinkage) can be handled via the latent-state construction in Theorem E.1 in online Appendix E.

### 4.3 Regularization

Regularization enters (i) during tree growth, (ii) during reconstruction from a fixed tree, and (iii) at the ensembling stage. When growing a tree, the optimization scheme regularizes through split selection and stopping rules (4); the Bayesian scheme regularizes through RUHWT priors and the latent states of Theorem E.1 (Section 2.3). During reconstruction, regularization acts directly on UH coefficients. In the optimization framework, we threshold coefficients as in (7) before reconstructing (cf. (5)); in the Bayesian framework, posterior means/draws of coefficients are shrunk by their priors, the likelihood, and latent states.

At the ensembling stage, boosting reduces the loss  $\frac{1}{n} \sum_{i=1}^n (y_i - f(\mathbf{x}_i))^2$  via updates (14), where each  $g_t$  in (16) is a residual-fitted UH tree with coefficient shrinkage, and  $\eta$  limits each tree's contribution. Bayesian backfitting uses the additive model (19)–(24), updating each component on the partial residual (21); as residuals shrink, later posterior draws concentrate near small trees with small coefficients, so the ensemble behaves like a structured shrinkage prior over many UH coefficients.

Classical tree ensembles regularize mainly via tree size (e.g., pruning) or leaf priors (Luo & Pratola 2022, Hastie & Pregibon 1990, Breiman et al. 1984, Zhang & Luo 2025). In contrast, UH ensembles always operate in orthogonal UH systems induced by the learned partitions and regularize explicitly at the split, coefficient, and ensemble stage using the same wavelet contrasts that drive (4), (5), and (19).

## 5 Theoretical Results

The recursive constructions on rectangular and triangulable domains use the same principle: starting with a base partition  $\mathcal{P}_0$  (typically with  $|\mathcal{P}_0| = 1$  cell for a rectangular domain or  $|\mathcal{P}_0| = 20$  cells for a spherical domain using an icosahedron base partition), each split of a cell creates two children and introduces exactly one new UH “detail” supported on the parent that is orthonormal in  $L^2(\mu)$ , where  $\mu = \mu_n$  is the empirical measure on the sample points. After all splits, we obtain a partition  $\mathcal{P}$  with  $|\mathcal{P}|$  cells and  $M = |\mathcal{P}| - |\mathcal{P}_0|$  non-constant UH details.

Let  $\mathcal{P} = \{A_1, \dots, A_{|\mathcal{P}|}\}$  be a partition obtained by admissible splits. Each split  $s: A \rightarrow (A_1, A_2)$  defines an UH atom

$$\psi_s = \sqrt{\frac{\mu(A_1)\mu(A_2)}{\mu(A)}} \left( \frac{\mathbf{1}_{A_1}}{\mu(A_1)} - \frac{\mathbf{1}_{A_2}}{\mu(A_2)} \right), \quad \langle \psi_s, 1 \rangle_{L^2(\mu)} = 0, \quad \|\psi_s\|_{L^2(\mu)} = 1.$$

Collecting all such atoms for  $\mathcal{P}$  gives  $\{\psi_j\}_{j=1}^M$ , which, together with the constant, span the piecewise-constant functions on  $\mathcal{P}$ . For each  $j = 1, \dots, M$ , let  $w_j = \langle Y, \psi_j \rangle_{L^2(\mu)}$ . For any  $S \subset \{1, \dots, M\}$ , let  $f_S$  be the  $L^2(\mu)$ -projection of  $f$  onto  $\text{span}\{\psi_j: j \in S\}$ , which means that at most  $|S|$  out of all possible wavelet basis functions have non-zero coefficients.

**Theorem 5.1** (Oracle bounds on a fixed partition). *Let  $(\mathcal{D}, \nu)$  be either a rectangular grid with its reference measure or a triangulable domain with the empirical measure on the sample points. Let the recursive rule of this paper produce a partition  $\mathcal{P}$  and corresponding orthonormal UH details  $\{\psi_j\}_{j=1}^M$  as above. Fix  $\mathcal{P}$  and  $0 < \delta < 1$ , and set*

$$\tau = \sigma \sqrt{\frac{2}{n} \log \frac{2M}{\delta}}. \quad (25)$$

*The soft-thresholded UH estimator*

$$\hat{f}_{\mathcal{P}, \tau}^{\text{UH}}(\mathbf{x}) = \bar{Y} + \sum_{j=1}^M \text{sgn}(w_j) \left( |w_j| - \tau \right)_+ \psi_j(\mathbf{x}), \quad \bar{Y} = \int Y d\mu, \quad w_j = \langle Y, \psi_j \rangle_{L^2(\mu)},$$

*satisfies, with probability at least  $1 - \delta$ ,*

$$\|\hat{f}_{\mathcal{P}, \tau}^{\text{UH}} - f\|_{L^2(\mu)}^2 \leq 4 \min_{S \subset \{1, \dots, M\}} \left\{ \|f - f_S\|_{L^2(\mu)}^2 + |S|\tau^2 \right\}. \quad (26)$$

*On the same partition, the leafwise (CART-style) estimator*

$$\hat{f}_{\mathcal{P}}^{\text{leaf}}(\mathbf{x}) = \frac{1}{N_A} \sum_{i: \mathbf{x}_i \in A} Y_i, \quad \mathbf{x} \in A \in \mathcal{P},$$

*satisfies, with probability at least  $1 - \delta$ ,*

$$\|\hat{f}_{\mathcal{P}}^{\text{leaf}} - f\|_{L^2(\mu)}^2 \leq \|f - f_{\mathcal{P}}\|_{L^2(\mu)}^2 + 4 \frac{\sigma^2}{m_{\min}(\mathcal{P})} \log \left( \frac{2|\mathcal{P}|}{\delta} \right), \quad (27)$$

*where  $f_{\mathcal{P}}$  is the piecewise-constant projection of  $f$  on  $\mathcal{P}$  and  $m_{\min}(\mathcal{P}) = \min_{A \in \mathcal{P}} N_A$ . If  $f$  is Hölder- $\alpha$  on each  $A$  with constant  $L_f$ , then  $\|f - f_{\mathcal{P}}\|_{L^2(\mu)}^2 \leq L_f^2 \sum_{A \in \mathcal{P}} h_A^{2\alpha} \mu(A)$ .*

Inequality (26) shows that, on any fixed tree partition, UH soft thresholding automatically adapts to the sparsity of  $f$  in the UH dictionary: if  $f$  is well approximated by a small set  $S$  of coefficients, the risk scales like  $|S|/n$  (up to logarithms). In contrast, (27) shows that the stochastic term for leafwise means depends on the smallest leaf size, and effectively on the total number of leaves. This supports our use of UH thresholding inside each tree in Sections 2 and 4: once a tree is grown, we reconstruct via (5) but only with coefficients that pass a threshold, which is exactly the regime where (26) is favorable.

Finally, we state a simplified consequence of Theorem 5.1 that highlights the benefits of UH thresholding when the true signal is sparse in the UH dictionary.

**Corollary 5.2** (Sparse detail vectors). *Assume the setting of Theorem 5.1 on a fixed partition  $\mathcal{P}$ , and that  $f$  is exactly supported on a set  $S^*$  of UH atoms with  $s = |S^*| \ll M$ , so  $f = f_{S^*}$ . Assume also that every cell contains at least a constant fraction  $c \in (0, 1/2)$  of  $n/|\mathcal{P}|$  points. Then, for the UH estimator  $\hat{f}_{\mathcal{P}, \tau}^{\text{UH}}$  with  $\tau$  as in (25) and the leafwise estimator  $\hat{f}_{\mathcal{P}}^{\text{leaf}}$  in (27), with probability at least  $1 - \delta$ ,*

$$\|\hat{f}_{\mathcal{P}, \tau}^{\text{UH}} - f\|_{L^2(\mu)}^2 \leq 8s \frac{\sigma^2}{n} \log \frac{2M}{\delta}, \quad \|\hat{f}_{\mathcal{P}}^{\text{leaf}} - f\|_{L^2(\mu)}^2 \leq \frac{4}{c} |\mathcal{P}| \frac{\sigma^2}{n} \log \frac{2|\mathcal{P}|}{\delta}.$$

This corollary formalizes the advantage of reconstruction-time UH thresholding in scenarios where the signal is concentrated on a few nodes, such as localized bumps or spikes (including functions like Easom-type examples mentioned in Section 2). On a fixed tree,  $\hat{f}_{\mathcal{P},\tau}^{\text{UH}}$  pays variance proportional to the number of large coefficients  $s$ , whereas leafwise means pay variance proportional to the total number of leaves  $|\mathcal{P}|$ . In our ensemble constructions, each boosting step or backfitting component performs exactly this kind of coefficient selection on its own residuals, so the same sparse-versus-dense gap appears componentwise. Taken together, Theorem 5.1 and Corollary 5.2 provide the theoretical backing for both pillars: UHWTs offer a sparsity-adaptive, orthogonal representation on adaptive partitions, and this structure survives when we move from single trees to additive ensembles and from Euclidean grids to triangulable manifolds.

## 6 Numerical Experiments

This section will illustrate our methodology using simulated data on the image and sphere domains, and real data on the sphere domain. We will relegate our numerical experiments on tensor data to online Appendix L.2, and our real-data image and additional spherical simulations to respective online Appendix L.1 and online Appendix L.3.

### 6.1 BH versus UH for boosted ensembles on images

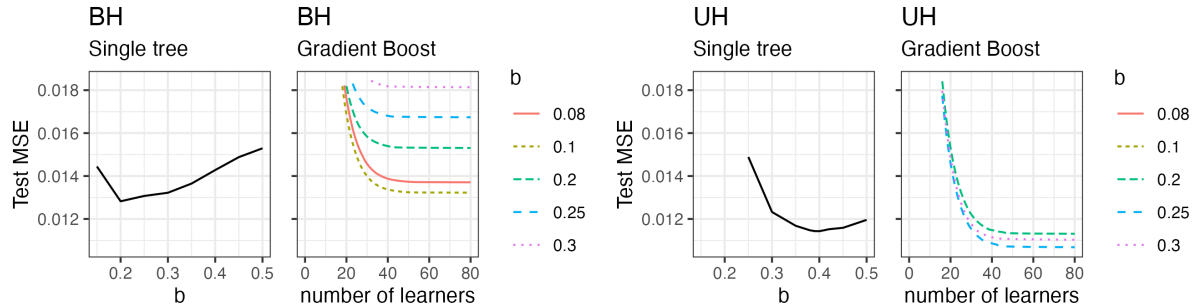


Figure 4: Metrics of methods fit to a  $512 \times 512$  pixel astronaut image with additive Gaussian noise whose standard deviation equals the noiseless image’s standard deviation. For each boosted ensemble, the learning rate is 0.1. The hyperparameter  $b$  is as defined at the beginning of Sec 6.1. For the fourth panel, the test MSEs for  $b \in \{0.08, 0.1\}$  were larger than 0.018 and hence are not shown.

This experiment illustrates the need for weak learners in a boosted ensemble to be able to split away from the midpoint. For each tree, we will stop splitting any node whose wavelet coefficient (3) is smaller than the threshold  $\tau = b\hat{\sigma}$  (Donoho 1995) for a user-defined hyperparameter  $b \geq 0$ . For both BH and UH trees and various values of  $b$ , we fit a single-tree learner and boosting ensembles to a  $512 \times 512$  pixel astronaut image with additive Gaussian noise whose standard deviation equals the noiseless image’s standard deviation.

Figure 4 shows the test MSE for the fitted models. The left two panels show that boosting using BH weak learners does not seem to reduce test MSE compared to a single BH tree: the

smallest BH single-tree test MSE is  $\approx 0.0129$  (at  $b = 0.2$ ), which is smaller than any of the boosting test MSEs with BH weak learners (we computed these test MSEs also for  $b = 0.09$  and  $b = 0.11$ , but omitted their MSE curves to avoid visual clutter). This supports the notion that boosting will not be effective if the weak learners always split at the midpoint. On the other hand, the third panel shows that the smallest UH single-tree test MSE is approximately 0.0114 (at  $b \approx 0.4$ ), which is noticeably larger than some of the shown (fourth panel) boosting test MSEs with UH weak learners, namely with  $b \in \{0.25, 0.3\}$ ; this implies that boosting can improve upon single-tree learners if learners are allowed to split away from the midpoint. Furthermore, the optimal value of  $b$  for a single-tree learner is larger than that for a boosted ensemble with learning rate 0.1; the learning rate allows the trees to grow deeper without as much risk of overfitting as when using a single-tree learner.

## 6.2 Numerical results for sphere: Beyond Matérn kernels

Here we illustrate our spherical methodology proposed in Section 4.1 on simulated data. The training data consist of  $n = 300$  i.i.d. data points  $(\mathbf{x}_i, y_i)$ ,  $i = 1, \dots, n$ , where the locations  $\mathbf{x}_i \in \mathbb{S}_2$  are drawn uniformly on a unit sphere, and the observed  $y_i$  are noisy versions of the unseen signal defined in the caption of Figure 5. Predictive performance is assessed by the MSE of the trained model on 15300 test sample points.

Although [Blaser & Fryzlewicz \(2016\)](#) mentioned the idea of incorporating random rotations into a boosted ensemble, we are not aware of any public implementation. We thus implement a *Random-Rotation Boosting* approach whose base learner will be our sphere wavelet, as described in Section 4.1. For comparison, we will also use a Fréchet tree ([Capitaine et al. 2024](#)) as a base learner, which we believe has never been publicly implemented before; we will call this approach *Random-Rotation Fréchet Boosting*.

We also compare our approach against existing tree-ensemble methods that allow inputs that lie on a sphere, namely Fréchet Forest ([Capitaine et al. 2024](#)), Random-Rotation Random Forest (called Random-Rotation Ensembles in [Blaser & Fryzlewicz \(2016\)](#)), and spherical PCA ([Luo et al. 2024](#)) with Rotation-Forest ([Rodriguez et al. 2006](#)). For Fréchet Forest, we used the `FrechForest` R package implementation. We also compare against three state-of-the-art nonparametric residual deep Gaussian process (GP) models ([Wyrwal et al. 2025](#)), which can model manifold- and scalar-valued functions with inputs supported on a manifold. [Wyrwal et al. \(2025\)](#) can be considered as a deep ensemble extension of [Gramacy \(2005\)](#) to spherical domains, with more sophisticated covariance and possible manifold uncertainty quantification ([Luo & Strait 2024](#)).

Figure 5 show the tree-ensemble predictions. The rotations smooth out the artificial boundaries or striations found in the predictions without rotations. Interestingly, the rotations increase the test MSE for the ensembles whose base learner is a Fréchet tree, but decrease the test MSE for the ensembles whose base learner is our wavelet tree using `adapt`. The rotations seem to increase the bias and variance of each base learner for the sake of increasing diversity between learners; we explore this phenomenon in online Appendix L.3.1. Our Random-Rotation Boosting approach produces the smallest test MSE among the tested methods, including the residual deep GP models whose MSEs are shown in Table 2; this was also observed for different signals, as described in online Appendices L.3.3 and L.3.4, as well as in the real-data example in Section 6.3. Furthermore, a spherical wavelet tree can

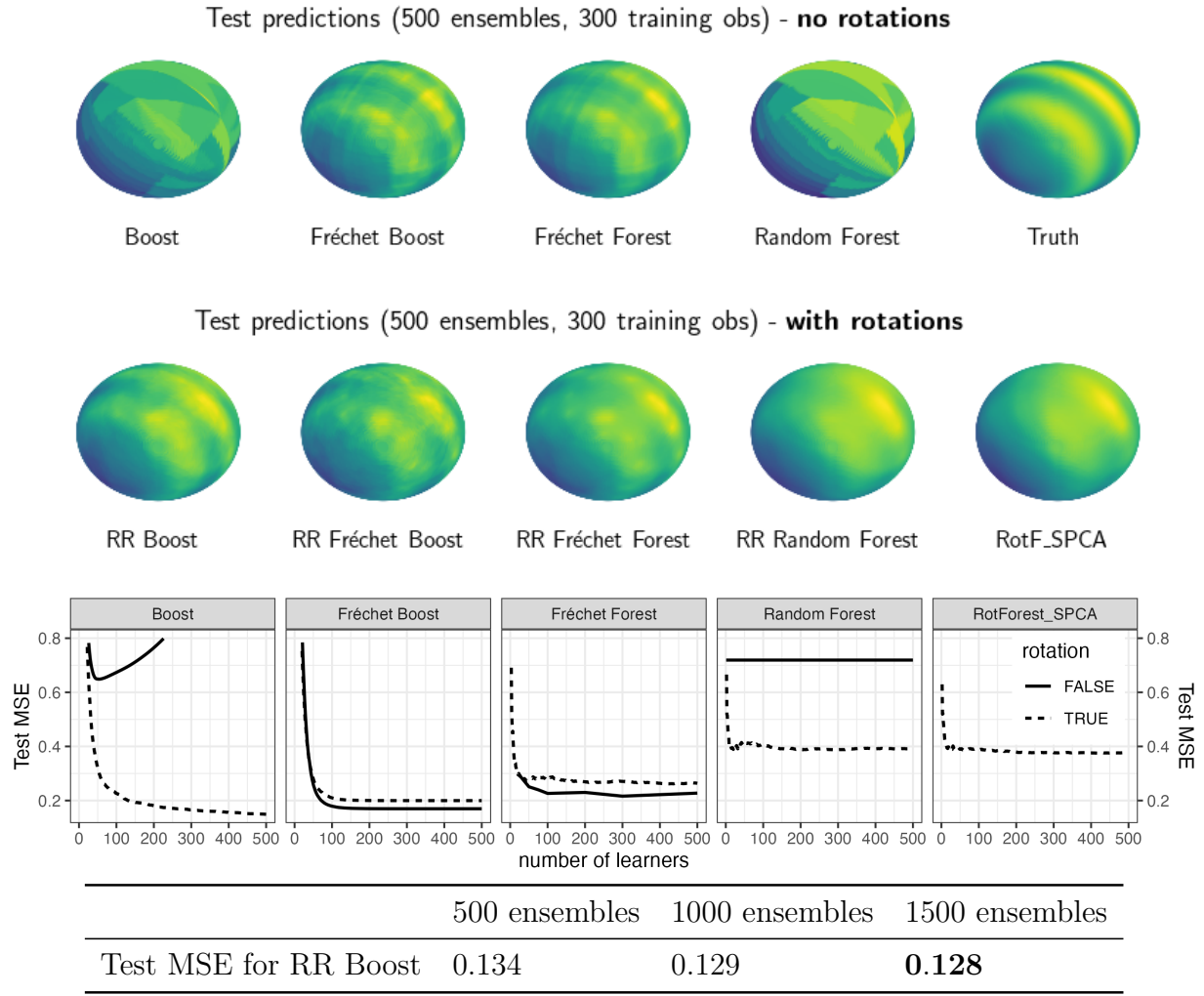


Figure 5: Empirical comparison of various tree ensemble models (“RR” refers to the method version that randomly rotates covariates before fitting any base learner) trained on  $n = 300$  points  $(\mathbf{x}, y)$ , where each location  $\mathbf{x} = (x_1, x_2, x_3)$  was drawn uniformly on the unit sphere, and the observed response  $y$  at  $\mathbf{x}$  is the signal  $f(\mathbf{x}) = 2 \tanh(x_1) + \cos(10x_2) + 2x_3$  plus i.i.d. Gaussian noise with zero mean and standard deviation equal to 0.1 of the standard deviation of  $f$ . Trees are allowed to grow to full depth. Boosted methods use learning rate 0.05. Top two rows: predictions of the ensemble methods. The true signal is shown in the top-right sphere. Third row: MSE on 15300 test points.

be applied to generic topological triangulations and hence can be used for a larger class of input domains than a Fréchet tree can, which requires inputs to lie on a metric space.

Finally, Table 3 shows the predictive improvement attained by incorporating a modest amount of soft thresholding into the Random-Rotation Boosting wavelets. Here we use the same functions, but we increase the sample size from 300 to 1000 to allow the trees to grow deep enough for soft thresholding to nontrivially affect the final prediction. We also increase the noise standard deviation to 0.3 of the standard deviation of  $f$ .

Test MSE	1 layer	2 layers	3 layers	4 layers
+hodge+spherical_harmonic_features	0.467 (0)	0.466 (0.000)	0.466 (0.000)	0.466 (0.000)
+inducing_points	0.466 (0.001)	0.208 (0.091)	0.209 (0.093)	0.207 (0.093)
+spherical_harmonic_features	0.467 (0)	<b>0.182 (0.010)</b>	0.192 (0.027)	0.199 (0.017)

Table 2: Mean and standard deviation of test MSE for three residual deep GP methods over 10 starting seeds (with variance provided in brackets), with different combinations of parameters as in their codebase. Data is described in Figure 5. Smallest MSE is bolded.

Function	soft 0.0	soft 0.1	soft 0.2	soft 0.3	soft 0.4
from Figure 5	0.0227	0.0218	<b>0.0217</b>	0.0224	0.0239
from online Appendix L.3.3	0.1033	0.1006	0.0989	<b>0.0981</b>	0.0983
from online Appendix L.3.4	$1.39 \times 10^{-3}$	<b><math>1.37 \times 10^{-3}</math></b>	$1.60 \times 10^{-3}$	$2.08 \times 10^{-3}$	$2.68 \times 10^{-3}$

Table 3: Test MSE for RR Boost trained on data from functions described in the stated figures, except that  $n = 1000$  and the noise standard deviation is equal to 0.3 of that of  $f$ .

### 6.3 Real data: GISS

Here we apply these spherical methods to real data that lie on the Earth. This example uses data from GISS Surface Temperature Analysis (GISSTEMP Team 2025, Lenssen et al. 2024), which is an estimate of global surface temperature change at various longitude-latitude coordinates of the Earth. Using data from the year 2023, we aim to predict the temperature change on a testing set (7766 observations) by training on 1941 other observations. Figure 6 shows the ensembles’ predictions and MSEs on the test data. Similarly to the simulated examples in Section 6.2 in the main text and online Appendix L.3, Figure 6 shows that the smallest test MSE is produced by the Random-Rotation Boosted ensemble and appears to further decrease if the number of learners increases, whereas the other methods appear to stabilize in their predictive performance. We also see that the prediction error appears to be largest at land-ocean borders, particularly near central America and northeastern Europe.

## 7 Conclusion

This work develops a wavelet regression framework built on two pillars. The first is an adaptive UHWT representation for regression whose transform is constructed directly in  $L^2(\mu_n)$ , so each admissible split is scored by its empirical UH coefficient and the selected atoms remain orthonormal (Section 2). The second pillar extends these constructions from regular grids to higher-order tensors and triangulable manifolds (Section 3). On spheres and general triangulated surfaces, we replace axis-aligned splits by geodesic triangle refinements that preserve local orthogonality in  $L^2(\mu_n)$ . Random rotations on  $\mathbb{S}^2$  and intrinsic reparameterizations on general manifolds generate diverse weak learners.

These two pillars come together in the ensemble constructions of Section 4. In the boosting procedure, each weak learner is an UH tree iteratively fitted to residuals and regularized by early stopping, a learning rate, and reconstruction-time soft thresholding. In the Bayesian

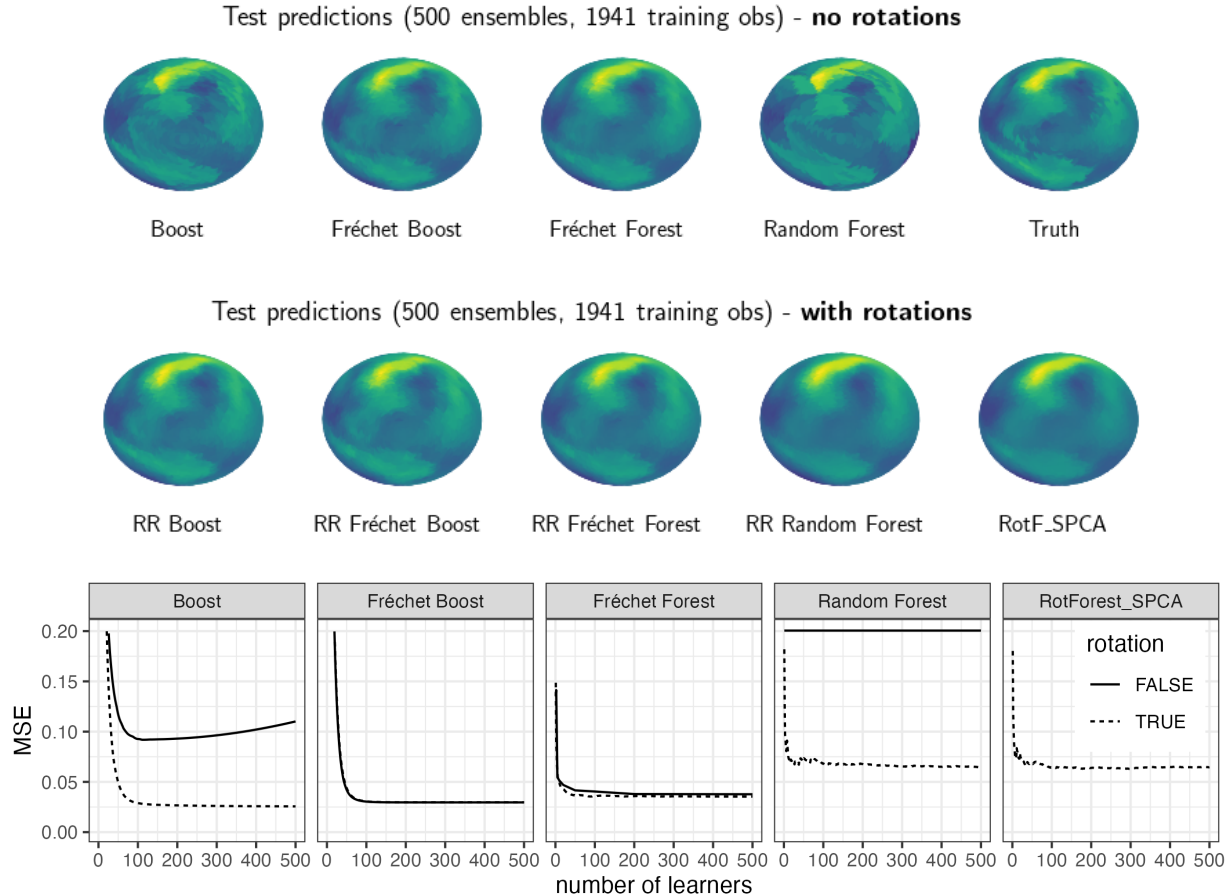


Figure 6: Empirical comparison of tree ensemble models (“RR” refers to the method version that randomly rotates covariates before fitting a base learner) trained on  $n = 1941$  points  $(x, y)$  from the GISS dataset. Trees are allowed to grow to full depth. Boosted methods use learning rate 0.05. Top two rows: predictions of the ensemble methods. The 7766 test points are shown in the top-right sphere. Third row: MSE on 7766 test points.

backfitting procedure, additive UH trees with RUHWT priors provide a fully probabilistic ensemble and uncertainty quantification for triangulable manifolds (Luo & Strait 2024), where each component sees only a partial residual and is shrunk by both its prior and its role in the sum.

Theoretical results in Section 5 support these design choices. Oracle inequalities for fixed partitions show that UH thresholding adapts to sparsity in the UH coefficients, with risk controlled by the number of large coefficients rather than the total number of leaves. A unified oracle bound covers both grids and triangulable domains once orthonormality with respect to the underlying measure is ensured. Together with the empirical results in Section 6 (and in the Supplementary Materials), these findings suggest that UH wavelet trees and their ensembles offer a practical and theoretically grounded tool for multiscale regression on complex domains, complementing classical grid-based wavelets and traditional tree ensembles.

## References

Agarwal, A., Tan, Y. S., Ronen, O., Singh, C. & Yu, B. (2022), Hierarchical shrinkage: Improving the accuracy and interpretability of tree-based models., in ‘International Conference on Machine Learning’, PMLR, pp. 111–135.

Blaser, R. & Fryzlewicz, P. (2016), ‘Random rotation ensembles’, *The Journal of Machine Learning Research* **17**(1), 126–151.

Breiman, L. (2001), ‘Random forests’, *Machine learning* **45**, 5–32.

Breiman, L., Friedman, J., Olshen, R. & Stone, C. (1984), *Classification and Regression Trees*, Wadsworth, Inc.

Bulté, M. & Sørensen, H. (2024), ‘Medoid splits for efficient random forests in metric spaces’, *Computational Statistics & Data Analysis* **198**, 107995.

Capitaine, L., Bigot, J., Thiébaut, R. & Genuer, R. (2024), ‘Fréchet random forests for metric space valued regression with non euclidean predictors’, *Journal of Machine Learning Research* **25**(355), 1–41.

Chipman, H. A., George, E. I. & McCulloch, R. E. (2010), ‘Bart: Bayesian additive regression trees’, *The Annals of Applied Statistics* **4**(1), 266–298.

Coifman, R. R. & Donoho, D. L. (1995), *Translation-invariant de-noising*, Springer.

Daubechies, I. (1992), ‘Ten lectures on wavelets’, *Society for industrial and applied mathematics* .

Donoho, D. L. (1995), ‘De-noising by soft-thresholding’, *IEEE transactions on information theory* **41**(3), 613–627.

Donoho, D. L. (1997), ‘CART and best-ortho-basis: a connection’, *The Annals of statistics* **25**(5), 1870–1911.

Donoho, D. L., Johnstone, I. M., Kerkyacharian, G. & Picard, D. (1995), ‘Wavelet shrinkage: asymptopia?’, *Journal of the Royal Statistical Society: Series B (Methodological)* **57**(2), 301–337.

Edelsbrunner, H. & Shah, N. R. (1994), Triangulating topological spaces, in ‘Proceedings of the tenth annual symposium on Computational geometry’, pp. 285–292.

Fang, L., Li, S., Cunefare, D. & Farsiu, S. (2016), ‘Segmentation based sparse reconstruction of optical coherence tomography images’, *IEEE transactions on medical imaging* **36**(2), 407–421.

Friedman, J. H. (2001), ‘Greedy function approximation: A gradient boosting machine’, *The Annals of Statistics* **19**, 1189–1232.

Friedman, J. H. & Tukey, J. W. (1974), ‘A projection pursuit algorithm for exploratory data analysis’, *IEEE Transactions on computers* **100**(9), 881–890.

Fryzlewicz, P. (2007), ‘Unbalanced Haar technique for nonparametric function estimation’, *Journal of the American Statistical Association* **102**(480), 1318–1327.

Fryzlewicz, P. & Timmermans, C. (2016), ‘Shah: Shape-adaptive haar wavelets for image processing’, *Journal of Computational and Graphical Statistics* **25**(3), 879–898.

GISTEMPTeam (2025), ‘Giss surface temperature analysis (gistemp), version 4’, NASA Goddard Institute for Space Studies. Dataset accessed 2025-07-08 at <https://data.giss.nasa.gov/gistemp/>.

Gramacy, R. B. (2005), *Bayesian treed Gaussian process models*, University of California, Santa Cruz.

Hastie, T. & Pregibon, D. (1990), *Shrinking trees*, AT & T Bell Laboratories.

Hastie, T. & Tibshirani, R. (2000), ‘Bayesian backfitting (with comments and a rejoinder by the authors)’, *Statistical Science* **15**(3), 196–223.

Hui, K.-H., Li, R., Hu, J. & Fu, C.-W. (2022), Neural wavelet-domain diffusion for 3d shape generation, in ‘SIGGRAPH Asia 2022 Conference Papers’, pp. 1–9.

Klusowski, J. M. & Tian, P. M. (2024), ‘Large scale prediction with decision trees’, *Journal of the American Statistical Association* **119**(545), 525–539.

Kolaczyk, E. D. & Nowak, R. D. (2005), ‘Multiscale generalised linear models for nonparametric function estimation’, *Biometrika* **92**(1), 119–133.

Lenssen, N., Schmidt, G. A., Hendrickson, M., Jacobs, P., Menne, M. J. & Ruedy, R. (2024), ‘A gistempv4 observational uncertainty ensemble’, *Journal of Geophysical Research: Atmospheres* **129**(17).

Li, M. & Ghosal, S. (2015), ‘Fast translation invariant multiscale image denoising’, *IEEE Transactions on Image Processing* **24**(12), 4876–4887.

Li, M. & Ma, L. (2021), ‘Learning asymmetric and local features in multi-dimensional data through wavelets with recursive partitioning’, *IEEE Transactions on Pattern Analysis and Machine Intelligence* **44**(11), 7674–7687.

Luo, H., Horiguchi, A. & Ma, L. (2025), ‘Efficient decision trees for tensor regressions’, *Journal of Computational and Graphical Statistics* pp. 1–14.

Luo, H. & Pratola, M. T. (2022), ‘Sharded Bayesian Additive Regression Trees’, *arXiv:2306.00361* pp. 1–46.

Luo, H., Purvis, J. E. & Li, D. (2024), ‘Spherical Rotation Dimension Reduction with Geometric Loss Functions’, *Journal of Machine Learning Research* **25**(175), 1–55.

Luo, H. & Strait, J. D. (2024), ‘Multiple closed curve modeling with uncertainty quantification for shape analysis’, *SIAM/ASA Journal on Uncertainty Quantification* **12**(4), 1192–1212.

Luo, Z. T., Sang, H. & Mallick, B. (2021), ‘Bast: Bayesian additive regression spanning trees for complex constrained domain’, *Advances in Neural Information Processing Systems* **34**, 90–102.

Luo, Z. T., Sang, H. & Mallick, B. (2022), Bamdt: Bayesian additive semi-multivariate

decision trees for nonparametric regression, in ‘International Conference on Machine Learning’, PMLR, pp. 14509–14526.

Mallat, S. G. (1989), ‘A theory for multiresolution signal decomposition: the wavelet representation’, *IEEE transactions on pattern analysis and machine intelligence* **11**(7), 674–693.

Mallat, S. G. (1999), *A wavelet tour of signal processing*, Elsevier.

Meinshausen, N. & Ridgeway, G. (2006), ‘Quantile regression forests.’, *Journal of machine learning research* **7**(6).

Mostowsky, P., Dutordoir, V., Azangulov, I., Jaquier, N., Hutchinson, M. J., Ravuri, A., Rozo, L., Terenin, A. & Borovitskiy, V. (2024), ‘The GeometricKernels Package: Heat and Matérn Kernels for Geometric Learning on Manifolds, Meshes, and Graphs’, *arXiv:2407.08086* .

Nason, G. P. (2008), *Wavelet methods in statistics with R*, Springer.

Rodriguez, J. J., Kuncheva, L. I. & Alonso, C. J. (2006), ‘Rotation forest: A new classifier ensemble method’, *IEEE transactions on pattern analysis and machine intelligence* **28**(10), 1619–1630.

Schröder, P. & Sweldens, W. (1995), Spherical wavelets: Efficiently representing functions on the sphere, in ‘Proceedings of the 22nd annual conference on Computer graphics and interactive techniques’, pp. 161–172.

Scornet, E., Biau, G. & Vert, J.-P. (2015), ‘Consistency of random forests’, *The Annals of Statistics* **43**(4), 1716–1741.

Sparapani, R., Spanbauer, C. & McCulloch, R. (2021), ‘Nonparametric machine learning and efficient computation with Bayesian additive regression trees: The BART R package’, *Journal of Statistical Software* **97**(1), 1–66.

Wager, S. & Athey, S. (2018), ‘Estimation and inference of heterogeneous treatment effects using random forests’, *Journal of the American Statistical Association* **113**(523), 1228–1242.

Wyrwal, K., Krause, A. & Borovitskiy, V. (2025), Residual deep gaussian processes on manifolds, in ‘The Thirteenth International Conference on Learning Representations’.

Xie, J., Lu, Y., Zhu, S.-C. & Wu, Y. N. (2016), ‘Inducing wavelets into random fields via generative boosting’, *Applied and Computational Harmonic Analysis* **41**(1), 4–25.

Zhang, Z. & Luo, H. (2025), ‘Minimax decision trees via martingale approximations’, *arXiv preprint arXiv:2502.16758* .

Zhou, M., Chen, H., Paisley, J., Ren, L., Li, L., Xing, Z., Dunson, D., Sapiro, G. & Carin, L. (2011), ‘Nonparametric bayesian dictionary learning for analysis of noisy and incomplete images’, *IEEE Transactions on Image Processing* **21**(1), 130–144.

# SUPPLEMENTARY MATERIAL

References from the main text will be preceded by “MT.”

## A Related Algorithms

---

**Input:** Data  $\{(\mathbf{x}_i, y_i)\}_{i=1}^n$  on domain  $\Omega \subset \mathbb{R}^D$ . Hyperparameters: maximum depth  $L_{\max}$ , minimum leaf size  $n_{\min} \in \mathbb{N}$ , and contrast threshold  $\tau$  (e.g.  $\tau = \tau_{n,\delta}$ ).

**Output:** A UH tree  $T$  (i.e., a recursive partition  $\mathcal{P}(T)$ ) whose internal nodes store a split  $(\hat{d}, \hat{\ell})$  and UH detail coefficients; reconstruction uses (MT-5).

**Notation.** For any node/cell  $A \subset \Omega$ , let  $I_A := \{i : \mathbf{x}_i \in A\}$  and  $N_A := |I_A|$ . For a split candidate  $(d, \ell)$  (coordinate  $d \in \{1, \dots, D\}$  and threshold  $\ell \in \mathbb{R}$ ), let  $A_l(d, \ell)$  and  $A_r(d, \ell)$  be the two children induced by the split (as in Section MT-2.2), and let  $w_{d,\ell}(A)$  be the UH contrast defined in (3).

**Procedure.**

1. *Initialize.* Set the root node  $A_0 \leftarrow \Omega$  and  $T \leftarrow \{A_0\}$ .
2. *While* there exists a leaf  $A \in T$  with  $\text{depth}(A) < L_{\max}$ , process  $A$  (e.g. breadth-first):
  - (a) *Admissible splits.* For each  $d \in \{1, \dots, D\}$ , form the set of admissible thresholds  $\Lambda_A(d)$  consisting of values of  $\{x_{i,d} : i \in I_A\}$  whose split produces children with  $N_{A_l(d,\ell)} \geq n_{\min}$  and  $N_{A_r(d,\ell)} \geq n_{\min}$ .
  - (b) *Score candidates.* Compute  $w_{d,\ell}(A)$  from (MT-3) for all admissible  $(d, \ell)$ .
  - (c) *Split or stop.* If no admissible  $(d, \ell)$  exists or  $\max_{(d,\ell)} |w_{d,\ell}(A)| < \tau$ , mark  $A$  as a leaf. Otherwise choose and store

$$(\hat{d}, \hat{\ell}) \in \arg \max_{(d,\ell)} |w_{d,\ell}(A)|, \quad (28)$$

split  $A$  into  $A_l(\hat{d}, \hat{\ell})$  and  $A_r(\hat{d}, \hat{\ell})$ , and add both children to  $T$ .

3. **Return**  $T$ .

**Prediction.** Reconstruct  $\hat{f}$  from the UH coefficients on  $T$  using (MT-5).

---

**Algorithm 1:** Optimization approach for fitting a single UHWT (aligned with (MT-3), (MT-4), and (MT-5)).

**Implementation notes for Algorithm 2.** Algorithm 2 is the greedy optimization procedure of Algorithm 1 specialized to  $\Omega = \mathbb{S}^2$  and evaluated in rotated ambient coordinates. Candidate splits remain axis-aligned in the rotated coordinate system (i.e.,  $X_{i,d} \leq \ell$ ), producing spherical caps/belts  $A_l(d, \ell)$  and  $A_r(d, \ell)$  within the current cell. The only implementation choice beyond the abstract description is the candidate set  $\Lambda_A(d)$  (controlled by `rule`); the split score and stopping rule use the same UH contrasts and threshold test  $\max_{(d,\ell)} |w_{d,\ell}(A)| < \tau$  as in the main text.

**A.0.0.1 Haar-uniform rotations on  $\text{SO}(3)$ .** To draw  $R \sim \text{Haar}(\text{SO}(3))$ , sample  $G \in \mathbb{R}^{3 \times 3}$  with i.i.d.  $\mathcal{N}(0, 1)$  entries, compute the QR factorization  $G = Q R_{\text{up}}$  with

---

**Input:** Locations  $X \in \mathbb{R}^{n \times 3}$  with rows on  $\mathbb{S}^2$ ; responses  $r \in \mathbb{R}^n$  (e.g., residuals or observed responses).

Hyperparameters  $\Theta = (L_{\max}, n_{\min}, \tau, \text{rule})$  with  $L_{\max}$  maximum depth,  $n_{\min}$  minimum leaf size,  $\tau \geq 0$  contrast threshold, and  $\text{rule} \in \{\text{balance}, \text{balance4}, \text{adapt}, \text{adapt\_vertex}\}$ . Initial icosahedron.

**Output:** For all  $j = 1, \dots, 20$ , a UH tree  $T^{(j)}$  (i.e., a partition  $\mathcal{P}(T^{(j)})$ ) on each face where  $T^{(j)}$ 's internal nodes store split decisions  $(\hat{d}, \hat{\ell})^{(j)}$  and UH detail coefficients (from (MT-3)).

**Notation.** For a node/cell  $A$ , let  $I_A \subset \{1, \dots, n\}$  be its index set,  $N_A := |I_A|$ , and  $\bar{r}_A := N_A^{-1} \sum_{i \in I_A} r_i$ . For a candidate  $(d, \ell)$  with  $d \in \{1, 2, 3\}$  and  $\ell \in \mathbb{R}$ , define children index sets

$$I_{A_l(d, \ell)} := \{i \in I_A : X_{i,d} \leq \ell\}, \quad I_{A_r(d, \ell)} := I_A \setminus I_{A_l(d, \ell)}, \quad (29)$$

and write  $N_{A_\bullet} := |I_{A_\bullet}|$  and  $\bar{r}_{A_\bullet}$  for the corresponding sizes and means. The UH contrast for  $(A; d, \ell)$  is

$$w_{d, \ell}(A) := \sqrt{\frac{N_{A_l(d, \ell)} N_{A_r(d, \ell)}}{N_A}} (\bar{r}_{A_l(d, \ell)} - \bar{r}_{A_r(d, \ell)}), \quad (30)$$

which matches (MT-3).

**Procedure.** For  $j = 1, \dots, 20$ :

1. *Initialize.* Denote by  $A_0^{(j)}$  the  $j$ th face of the icosahedron. Set  $T^{(j)} \leftarrow \{A_0^{(j)}\}$  and  $\text{depth}(A_0^{(j)}) = 0$ .

2. *While* there exists a leaf  $A \in T^{(j)}$  with  $\text{depth}(A) < L_{\max}$ , process  $A$ :

(a) *Admissible thresholds.* For each  $d \in \{1, 2, 3\}$ , define  $\Lambda_A(d)$  by

$$\Lambda_A(d) := \begin{cases} \{\text{empirical median of } \{X_{i,d}\}_{i \in I_A}\}, & \text{rule} = \text{balance}, \\ \{\text{empirical quartiles of } \{X_{i,d}\}_{i \in I_A}\}, & \text{rule} = \text{balance4}, \\ \{\text{midpoints of consecutive distinct values in } \{X_{i,d}\}_{i \in I_A}\}, & \text{rule} = \text{adapt}, \\ \{\text{distinct values in } \{X_{i,d}\}_{i \in I_A}\}, & \text{rule} = \text{adapt\_vertex}. \end{cases} \quad (31)$$

Discard any  $\ell \in \Lambda_A(d)$  violating  $N_{A_l(d, \ell)} \geq n_{\min}$  and  $N_{A_r(d, \ell)} \geq n_{\min}$ .

(b) *Score candidates.* Compute  $w_{d, \ell}(A)$  for all admissible  $(d, \ell)$ .

(c) *Split or stop.* If no admissible  $(d, \ell)$  exists or  $\max_{(d, \ell)} |w_{d, \ell}(A)| < \tau$ , mark  $A$  as a leaf. Otherwise choose and store

$$(\hat{d}, \hat{\ell}) \in \arg \max_{(d, \ell)} |w_{d, \ell}(A)|, \quad (32)$$

split  $A$  into  $A_l(\hat{d}, \hat{\ell})$  and  $A_r(\hat{d}, \hat{\ell})$ , and add both children to  $T^{(j)}$ .

3. **Return**  $T^{(j)}$ .

**Prediction.** For  $x \in A_0^{(j)}$ , use UH synthesis on  $T^{(j)}$ , as in (MT-5). (When used inside boosting,  $r$  is the stagewise residual and the resulting fit corresponds to the weak learner in (MT-16)–(MT-18).)

---

**Algorithm 2:** SPHEREPARTITIONERUH( $X, r; \Theta$ ): UH tree on  $\mathbb{S}^2$  data (notation aligned with (MT-3) and (MT-18)).

$Q^\top Q = I_3$ , and enforce  $Q \in \text{SO}(3)$  by a sign fix:

$$\tilde{Q} = Q \cdot \text{diag}(1, 1, \text{sign}(\det Q)), \quad \det(\tilde{Q}) = +1. \quad (41)$$

Then  $\tilde{Q}$  is Haar on  $\text{SO}(3)$ .

If a base tree is fit on rotated locations  $\{R\mathbf{x}_i\}$ , then test points must be mapped consistently to  $R\mathbf{x}$  before evaluating the UH reconstruction on that tree, matching (MT-18).

---

**Input:** Image array  $Y \in \mathbb{R}^{nr \times nc}$  on  $\Omega \subset \mathbb{R}^2$ ; maximum depth  $L_{\max}$ ; iterations  $K$ ; depth-based split prior  $p_{\text{split}}(d) = 0.99 \cdot 0.499^d$ ; noise level  $\sigma$  (MAD estimate if not supplied).

**Output:** A UH tree  $T$  (last accepted state) whose internal nodes store split  $(d, \ell)$  and UH details.

**Notation.** For a node  $A$ , let  $\text{depth}(A)$  be its depth. When  $A$  is internal with stored  $(d, \ell)$ , write  $w_{d, \ell}(A)$  for its UH contrast (as in (MT-3), specialized to the image grid).

**Initialization.** Set root  $A_0 = \Omega$ ,  $\text{depth}(A_0) = 0$ , and initialize  $T \leftarrow \{A_0\}$ .

**Local scores on a subtree rooted at  $A$ .**

- *Local prior:*

$$\log \pi_{\text{prior}}(A) = \sum_{U \in \text{Desc}(A) \cup \{A\}} \begin{cases} \log(1 - p_{\text{split}}(\text{depth}(U))), & U \text{ leaf}, \\ \log(p_{\text{split}}(\text{depth}(U))), & U \text{ internal}. \end{cases} \quad (33)$$

- *Local likelihood (Gaussian):*

$$\log \mathcal{L}(A) = \sum_{\substack{U \in \text{Descendants of}(A) \cup \{A\} \\ U \text{ internal}}} \log \phi_{\sigma}(w_{d_U, \ell_U}(U)) - \sum_{U \text{ leaf}} \frac{\text{SSE}(U)}{2\sigma^2}, \quad (34)$$

where  $\phi_{\sigma}$  is the  $N(0, \sigma^2)$  density and  $\text{SSE}(U)$  is the within-leaf sum of squares about the leaf mean.

- *Local log-posterior:*  $\log \Pi(A) := \log \pi_{\text{prior}}(A) + \log \mathcal{L}(A)$ .

**One MCMC step (repeat for  $t = 1, \dots, K$ ).**

1. Choose move type  $\text{move} \in \{\text{GROW}, \text{PRUNE}\}$  uniformly, for candidate sets:

$$\mathcal{C}_{\text{GROW}}(T) = \{U : U \text{ leaf and } \text{depth}(U) < L_{\max}\}, \quad (35)$$

$$\mathcal{C}_{\text{PRUNE}}(T) = \{U : U \text{ internal and both children are leaves}\}. \quad (36)$$

If  $\mathcal{C}_{\text{move}}(T) = \emptyset$ , switch  $\text{move}$  to the other move.

2. Pick target node  $A$  uniformly from  $\mathcal{C}_{\text{move}}(T)$  and compute  $L_{\text{cur}} = \log \Pi(A)$ .
3. Propose a local change at  $A$  (We implemented SWAP option as well):
  - If  $\text{move} = \text{GROW}$ : propose a split  $(d, \ell)$  for  $A$  (image-row or image-column direction), create two children, and assign their depths  $\text{depth}(A) + 1$ .
  - If  $\text{move} = \text{PRUNE}$ : remove both children of  $A$  and mark  $A$  as a leaf (clear  $(d, \ell)$ ).
4. Compute  $L_{\text{prop}} = \log \Pi(A)$  after the change and the Hastings correction:

$$\Delta_{\text{prop}} = \begin{cases} \log \frac{|\mathcal{C}_{\text{GROW}}(T)|}{|\mathcal{C}_{\text{PRUNE}}(T')|}, & \text{move} = \text{GROW}, \\ \log \frac{|\mathcal{C}_{\text{PRUNE}}(T)|}{|\mathcal{C}_{\text{GROW}}(T')|}, & \text{move} = \text{PRUNE}, \end{cases} \quad (37)$$

where  $T'$  is the proposed tree (used only to count candidates).

5. Metropolis–Hastings accept with probability  $\min\{1, \exp(\Lambda)\}$ ,  $\Lambda = (L_{\text{prop}} - L_{\text{cur}}) + \Delta_{\text{prop}}$ .

**Return.** The final accepted  $T$  (and optionally the stored trace of trees).

---

**Algorithm 3:** Bayesian MCMC sampler for a single RUHWT (image-specialized; notation aligned with Section MT-2.3 and with boosting learning rate  $\eta$ ).

## B Orthonormal UH Basis

Let  $\mu_n = \frac{1}{n} \sum_{i=1}^n \delta_{\mathbf{x}_i}$  be the empirical measure, and let  $\mathcal{T}^\circ$  be a finite binary partition of  $\Omega$  with root cell  $A_0$ . For each internal node  $A \in \mathcal{T}^\circ$ , let  $A_L$  and  $A_R$  denote its left and right children, and write  $\mu_n(A) = \int_A d\mu_n = \frac{1}{n} \sum_{i=1}^n \mathbf{1}\{\mathbf{x}_i \in A\}$  for the empirical mass of  $A$ .

---

**Input:** Training data  $\{(y_i, \mathbf{x}_i)\}_{i=1}^n$  with  $\mathbf{x}_i \in \mathbb{S}^2$  and  $y_i \in \mathbb{R}$ ; ensemble size  $m$ ; base-tree parameters  $\Theta$  for Algorithm 2. Initial icosahedron.

Rotation generator HaarSO(3) (Gaussian–QR with sign fix; see below).

**Output:** Rotations  $\{R_t\}_{t=1}^m \subset \text{SO}(3)$  and UH trees  $\{(T_t^{(1)}, \dots, T_t^{(20)})\}_{t=1}^m$ , where for each  $j = 1, \dots, 20$  the superscript  $(j)$  denotes the  $j$ th face of the icosahedron.

**Procedure.**

1. For  $t = 1, \dots, m$ :

(a) Draw  $R_t \sim \text{HaarSO}(3)$ .

(b) Fit  $(T_t^{(1)}, \dots, T_t^{(20)}) \leftarrow \text{SPHEREPARTITIONERUH}(\{R_t \mathbf{x}_i\}_{i=1}^n, (y_i)_{i=1}^n; \Theta)$ .

2. **Return**  $\{R_t\}_{t=1}^m$  and  $\{(T_t^{(1)}, \dots, T_t^{(20)})\}_{t=1}^m$ .

**Prediction.** For  $\mathbf{x} \in \mathbb{S}^2$ ,

$$\hat{f}(\mathbf{x}) = \frac{1}{m} \sum_{t=1}^m \hat{f}_{T_t^{(j)}}(R_t \mathbf{x}), \quad (38)$$

where  $j = j_{R_t}$  is the index of the icosahedron's face containing  $R_t \mathbf{x}$ , and  $\hat{f}_{T_t^{(j)}}$  denotes the UH reconstruction on the tree  $T_t^{(j)}$  (cf. (MT-5)).

---

**Algorithm 4:** RRE: Random Rotation Ensemble with UH base trees on  $\mathbb{S}^2$  (notation aligned with Section 4).

Define the scaling function and wavelet functions by

$$\phi_{A_0}(\mathbf{x}) := \frac{\mathbf{1}\{\mathbf{x} \in A_0\}}{\sqrt{\mu_n(A_0)}}, \quad (42)$$

$$\psi_A(\mathbf{x}) := \sqrt{\frac{\mu_n(A_L) \mu_n(A_R)}{\mu_n(A)}} \left( \frac{\mathbf{1}\{\mathbf{x} \in A_L\}}{\mu_n(A_L)} - \frac{\mathbf{1}\{\mathbf{x} \in A_R\}}{\mu_n(A_R)} \right), \quad A \in \mathcal{T}^\circ. \quad (43)$$

We equip  $L^2(\mu_n)$  with the inner product  $\langle f, g \rangle_n := \int f(\mathbf{x}) g(\mathbf{x}) d\mu_n(\mathbf{x})$ .

**Lemma B.1** (Orthonormality of the UH system). *The collection*

$$\mathcal{U} := \{\phi_{A_0}\} \cup \{\psi_A : A \in \mathcal{T}^\circ\}$$

is an orthonormal system in  $L^2(\mu_n)$ .

*Proof.* We first check that each element has unit  $L^2(\mu_n)$  norm and then verify pairwise orthogonality.

*Norms.* For the scaling function,

$$\|\phi_{A_0}\|_n^2 = \int \phi_{A_0}^2(\mathbf{x}) d\mu_n(\mathbf{x}) = \frac{1}{\mu_n(A_0)} \int \mathbf{1}\{\mathbf{x} \in A_0\} d\mu_n(\mathbf{x}) = \frac{\mu_n(A_0)}{\mu_n(A_0)} = 1.$$

---

**Input:**  $(\{\mathbf{x}_i\}_{i=1}^n, y)$  with  $\mathbf{x}_i \in \mathbb{S}^2$ ; stages  $G$ ; learning rate  $\eta \in (0, 1]$ ; base parameters  $\Theta$ ; rotation generator  $\text{HaarSO}(3)$ .

**Output:** Predictor  $\hat{f}_G$  of the form (MT-18).

**Procedure.**

1. Initialize  $f_0(\mathbf{x}) \equiv \bar{y}_\Omega$  and residuals  $r_{0,i} := y_i - f_0(\mathbf{x}_i)$ .

2. For  $t = 1, \dots, G$ :

(a) Draw  $R_t \sim \text{HaarSO}(3)$ .

(b) Fit a UHWT weak learner on rotated inputs:

$$T_t \leftarrow \text{SPHEREPARTITIONERUH}(\{R_t \mathbf{x}_i\}_{i=1}^n, \{r_{t-1,i}\}_{i=1}^n; \Theta), \quad (39)$$

and let  $g_t(\mathbf{x})$  be the corresponding UH reconstruction on  $T_t$  evaluated at  $R_t \mathbf{x}$  (cf. (MT-16)–(MT-18)).

(c) Update

$$f_t(\mathbf{x}) \leftarrow f_{t-1}(\mathbf{x}) + \eta g_t(\mathbf{x}), \quad r_{t,i} \leftarrow y_i - f_t(\mathbf{x}_i). \quad (40)$$

3. **Return**  $f_G$ .

---

**Algorithm 5:** RRB: Random Rotation Boosting with UH weak learners on  $\mathbb{S}^2$  (matched to (MT-15)–(MT-18)).

Fix an internal node  $A \in \mathcal{T}^\circ$  with children  $A_L, A_R$ . By definition (43),  $\psi_A$  is supported on  $A_L \cup A_R$  and takes the constant values

$$c_L := \sqrt{\frac{\mu_n(A_L) \mu_n(A_R)}{\mu_n(A)}} \frac{1}{\mu_n(A_L)} \quad \text{on } A_L, \quad c_R := -\sqrt{\frac{\mu_n(A_L) \mu_n(A_R)}{\mu_n(A)}} \frac{1}{\mu_n(A_R)} \quad \text{on } A_R.$$

Hence

$$\begin{aligned} \|\psi_A\|_n^2 &= \int \psi_A^2(\mathbf{x}) d\mu_n(\mathbf{x}) \\ &= \int_{A_L} c_L^2 d\mu_n(\mathbf{x}) + \int_{A_R} c_R^2 d\mu_n(\mathbf{x}) \\ &= c_L^2 \mu_n(A_L) + c_R^2 \mu_n(A_R) \\ &= \frac{\mu_n(A_L) \mu_n(A_R)}{\mu_n(A)} \left( \frac{1}{\mu_n(A_L)} + \frac{1}{\mu_n(A_R)} \right) \\ &= \frac{\mu_n(A_R)}{\mu_n(A)} + \frac{\mu_n(A_L)}{\mu_n(A)} \\ &= 1, \end{aligned}$$

since  $\mu_n(A) = \mu_n(A_L) + \mu_n(A_R)$ .

*Orthogonality with the scaling function.* Each wavelet  $\psi_A$  has zero  $\mu_n$ -mean:

$$\int \psi_A(\mathbf{x}) d\mu_n(\mathbf{x}) = c_L \mu_n(A_L) + c_R \mu_n(A_R) = 0. \quad (44)$$

Therefore

$$\langle \phi_{A_0}, \psi_A \rangle_n = \frac{1}{\sqrt{\mu_n(A_0)}} \int_{A_0} \psi_A(\mathbf{x}) d\mu_n(\mathbf{x}) = 0.$$

*Orthogonality between wavelets.* Let  $A, B \in \mathcal{T}^\circ$ ,  $A \neq B$ . Because  $\mathcal{T}^\circ$  is a binary tree, nodes  $A$  and  $B$  are either disjoint, or one node is strictly contained in the other.

If  $A$  and  $B$  are disjoint, then  $\psi_A \psi_B \equiv 0$  and hence  $\langle \psi_A, \psi_B \rangle_n = 0$ . Suppose instead that  $B \subset A$  (the case  $A \subset B$  is symmetric). Since  $B$  lies entirely inside one child of  $A$ , say  $B \subseteq A_L$ , the wavelet  $\psi_A$  is constant on  $B$  with value  $c_L$  as above. Thus

$$\langle \psi_A, \psi_B \rangle_n = \int_B \psi_A(\mathbf{x}) \psi_B(\mathbf{x}) d\mu_n(\mathbf{x}) = c_L \int_B \psi_B(\mathbf{x}) d\mu_n(\mathbf{x}) = 0,$$

because  $\psi_B$  has zero  $\mu_n$ -mean on its support, as shown above in (44).

This exhausts all possibilities, so every pair of distinct elements of  $\mathcal{U}$  is orthogonal, and each has unit norm. Therefore  $\mathcal{U}$  is orthonormal in  $L^2(\mu_n)$ .  $\square$

## C Connection to CART

This section explores the similarity between CART and the optimization approach to fitting a UHWT in the grid case. We first consider how the splits are chosen. On a grid, and when  $|\cdot|$  in (MT-3) counts design points, this reduction in squared error matches the CART criterion up to constants. The greedy rule (MT-4) therefore coincides with the usual CART split rule. For a candidate split  $s: A \rightarrow (A_1, A_2)$ , the empirical squared-error decrease for a leafwise estimator is

$$\begin{aligned} \Delta_Y(s) &= \sum_{i:X_i \in A} (Y_i - \bar{Y}_A)^2 - \sum_{i:X_i \in A_1} (Y_i - \bar{Y}_{A_1})^2 - \sum_{i:X_i \in A_2} (Y_i - \bar{Y}_{A_2})^2 \\ &= \frac{N_{A_1} N_{A_2}}{N_A} (\bar{Y}_{A_1} - \bar{Y}_{A_2})^2, \end{aligned} \tag{45}$$

which, on a grid, is exactly the square of the UH coefficient  $|w_{d,\ell}(A)|$  used in the optimization rule (MT-4). Thus the greedy UH split and the greedy CART split share the same basic objective.

The identity (45) shows that UH splitting is fully aligned with CART when the same candidate set is used: both rules pick the split that maximizes the drop in empirical risk, and the UH coefficient is simply a more convenient parameterization of that drop.

In the analysis of [Donoho \(1997\)](#), CART appears as a method for selecting an orthonormal basis from a predefined library. Here the same equality between reduction in squared error and squared UH coefficient is used in the opposite direction: the CART partition is interpreted as a sequence of UH atoms and thereby defines an orthogonal wavelet system in  $L^2(\mu_n)$  on the empirical design. Compared with the univariate UH construction in [Fryzlewicz \(2007\)](#), our optimization approach works in multiple dimensions, allows continuous split locations, and links the UH coefficients directly to the regression fit of a multivariate tree.

However, the reconstruction is different due to the regularization (MT-7). If the wavelet coefficients are not regularized (i.e., if  $\tilde{w}_{d,\ell}(A) = w_{d,\ell}(A)$  for all nodes  $A$ ), then (MT-5) yields the orthogonal projection of  $y$  onto the span of the selected UH atoms in  $L^2(\mu_n)$ .

**Theorem C.1.** *Let  $(\mathbf{x}_i, y_i)$  for  $i = 1, \dots, n$  be training data. Let  $\mathcal{Q}$  be a binary-tree partition of  $\Omega$ . For  $\mathbf{x} \in \Omega$  let  $A_{\mathbf{x}}$  denote the leaf of  $\mathcal{Q}$  that contains  $\mathbf{x}$  and define  $\hat{f}_{\mathcal{Q}}^{\text{leaf}}(\mathbf{x}) = n_{A_{\mathbf{x}}}^{-1} \sum_{\mathbf{x}_i \in A_{\mathbf{x}}} y_i$ , where  $n_{A_{\mathbf{x}}}$  is the number of training locations in  $A_{\mathbf{x}}$ . If  $\Omega$  is a grid and  $|\cdot|$  in (MT-3) equals the number of training locations in its argument, then  $\hat{f}_{\mathcal{Q}}^{\text{leaf}}$  equals  $\hat{f}_{\mathcal{Q}}^{\text{UH}}$  defined in (MT-5) when  $\tilde{w}_{d,\ell}(A) = w_{d,\ell}(A)$ .*

Therefore, the main difference between our optimization approach and tree-based regression algorithms such as CART lies in how the empirical estimate is regularized. CART regularizes by pruning subtrees, which can be interpreted as shrinking all coefficients in those subtrees to zero before applying (MT-5). In contrast, our approach regularizes by thresholding UH coefficients at each node using a threshold calibrated by a MAD estimate of the noise.

To motivate the use of wavelet regularization, we note that existing consistency results for CART (Scornet et al. 2015, Wager & Athey 2018, Klusowski & Tian 2024) often rely on no-interaction or smoothness conditions on  $f$  that are not well matched to the piecewise-constant and edge-driven structure of images and tensors. In contrast, UH-based estimators admit consistency for broader function classes in one dimension and for certain multiscale constructions (Fryzlewicz 2007, Kolaczyk & Nowak 2005). Empirically, Agarwal et al. (2022) also find (for non-grid domains) that CART’s predictive ability often improves when additional ( $L_2$ ) shrinkage is applied to an existing CART tree, even when it has already been pruned.

## D Proof of Theorem C.1

*Proof.* We will prove this claim by induction. For the base case, we have  $\hat{f}_{\mathcal{Q}}^{\text{leaf}} = \hat{f}_{\mathcal{Q}}^{\text{UH}}$  when  $\mathcal{Q} = \{\Omega\}$ , in which case the functions  $\hat{f}_{\mathcal{Q}}^{\text{leaf}}$  and  $\hat{f}_{\mathcal{Q}}^{\text{UH}}$  have constant value  $n_{\Omega}^{-1} \sum_{\mathbf{x}_i \in \Omega} y_i$ , i.e., the sample mean of the observed response values.

Now suppose  $\mathcal{P}$  is a binary-tree partition such that  $\hat{f}_{\mathcal{P}}^{\text{leaf}} = \hat{f}_{\mathcal{P}}^{\text{UH}}$ . For a leaf node  $A \in \mathcal{P}$ , suppose  $\mathcal{Q}$  is a binary-tree partition that is exactly  $\mathcal{P}$  except that  $A$  is an internal node in  $\mathcal{Q}$  with leaf nodes as children. By this assumption, we have

$$\hat{f}_{\mathcal{Q}}^{\text{leaf}}(\mathbf{x}) = \hat{f}_{\mathcal{P}}^{\text{leaf}}(\mathbf{x}) = \hat{f}_{\mathcal{P}}^{\text{UH}}(\mathbf{x}) = \hat{f}_{\mathcal{Q}}^{\text{UH}}(\mathbf{x}) \quad \text{for any } \mathbf{x} \notin A. \quad (46)$$

Now denote the left and right child of  $A$  as  $A_L$  and  $A_R$ , respectively. We have

$$\hat{f}_{\mathcal{Q}}^{\text{UH}}(\mathbf{x}) - \hat{f}_{\mathcal{Q}}^{\text{leaf}}(\mathbf{x}) = n_L \bar{y}_L \left[ -\frac{n_R}{n_L} \frac{1}{n_A} + \frac{|A_R|}{|A_L|} \frac{1}{|A|} \right] + n_R \bar{y}_R \left[ \frac{1}{n_A} - \frac{1}{|A|} \right] \quad \text{for any } \mathbf{x} \in A_L. \quad (47)$$

The RHS vanishes if  $|\cdot|$  is the number of training locations in the argument  $\cdot$ , in which case  $\hat{f}_{\mathcal{Q}}^{\text{leaf}}(\mathbf{x}) = \hat{f}_{\mathcal{Q}}^{\text{UH}}(\mathbf{x})$  for any  $\mathbf{x} \in A_L$ . Similar reasoning will imply that  $\hat{f}_{\mathcal{Q}}^{\text{leaf}}(\mathbf{x}) = \hat{f}_{\mathcal{Q}}^{\text{UH}}(\mathbf{x})$  for any  $\mathbf{x} \in A_R$ . Therefore,  $\hat{f}_{\mathcal{Q}}^{\text{leaf}} = \hat{f}_{\mathcal{Q}}^{\text{UH}}$ .  $\square$

## E Posterior distribution with latent states

The following theorem, Theorem E.1, extends Theorem MT-2.1 to incorporate latent states. (Our Theorem E.1 is also written in a way that emphasizes that a tree can be grown breadth-first or depth-first.) For tractability, the distribution of the latent states is modeled as a top-down Markov tree so that the state of a node can depend on the state of its parent but not on the state of any other node. For example, an early-stopping mechanism can be used: a node at depth  $j$  is no longer allowed to split with probability  $\rho_j$ , where  $\rho_j = 1$  if its parent is not allowed to split and  $\rho_j < 1$  if its parent is allowed to split; this mechanism can greatly reduce the bottom-up computation of  $\Phi_s(A)$  in Theorem E.1. Alternatively, a spike-and-slab framework enables a less stringent regularization approach: if a node is assigned to be a spike in order to indicate that its UH coefficient will be omitted when constructing the signal, then the probability that a node is a spike is allowed to depend on whether or not the node's parent is a spike.

**Theorem E.1.** *Suppose  $T$  has a RUHWT prior with split dimension probabilities  $\{\lambda_d(A): A \in \mathcal{A}, d \in \mathcal{D}(A)\}$  and split location distributions  $\{B_{A,d}: A \in \mathcal{A}, d \in \mathcal{D}(A)\}$  on  $[0, 1]$ , with zero probability of creating a child with no training locations. Suppose that, given  $T$  and hyperparameters  $\phi$ , the coefficients are conditionally independent given latent states  $\mathcal{S} = \{S_i \in \{1, \dots, K\}: A_i \in T\}$ :*

$$(w_i, z_i) \mid S(A_i) = s \stackrel{\text{ind}}{\sim} p_i^{(s)}(w, z \mid \phi), \quad A_i \in T. \quad (48)$$

*Assume that the distribution of the latent states follows a top-down Markov tree whose transition kernels  $P(S(A) = s' \mid S(A_p) = s) =: \rho_j(s, s')$ , where  $A_p$  is  $A$ 's parent, can depend on  $A$ 's depth  $j$  in the tree  $T$ . Then the joint marginal posterior of  $(T, \mathcal{S})$  admits the following sequential generative description.*

*We begin with  $k = 0$  and  $T^{(0)} = \{\Omega\}$ . Given a tree  $T^{(k)}$ , a node  $A \in T^{(k)}$  whose latent state has not yet been generated, and the latent state of  $A$ 's parent  $A_p$ , the state of  $A$  is drawn from*

$$P(S(A) = s' \mid S(A_p) = s, T^{(k)}, \mathbf{y}) = \rho_j(s, s') \sum_{d \in D(A)} \lambda_d(A) \int_0^1 M_{d,\ell}^{(s')}(A) \frac{\Phi_{s'}(A_l^{(d,\ell)}) \Phi_{s'}(A_r^{(d,\ell)})}{\Phi_s(A)} dB_{A,d}(\ell), \quad (49)$$

*where  $j$  is the depth of  $A$ . Given  $S(A) = s'$  and  $j < J$ , the split dimension and location of  $A$  are drawn from*

$$P(D(A) = d \mid S(A) = s', T^{(k)}, \mathbf{y}) \propto \lambda_d(A) \int_0^1 M_{d,\ell}^{(s')}(A) \Phi_{s'}(A_l^{(d,\ell)}) \Phi_{s'}(A_r^{(d,\ell)}) dB_{A,d}(\ell), \quad (50)$$

$$dB_{A,d}(\ell \mid D(A) = d, S(A) = s', T^{(k)}, \mathbf{y}) \propto dB_{A,d}(\ell) M_{d,\ell}^{(s')}(A) \Phi_{s'}(A_l^{(d,\ell)}) \Phi_{s'}(A_r^{(d,\ell)}), \quad (51)$$

*where  $M_{d,\ell}^{(s)}(A_i) := \int p_i^{(s)}(w_{d,\ell}(A_i), z \mid \phi) dz$ , and the state-specific marginal likelihood satisfies*

$$\Phi_s(A) = \sum_{s'} \rho_j(s, s') \sum_{d \in D(A)} \lambda_d(A) \int_0^1 M_{d,\ell}^{(s')}(A) \Phi_{s'}(A_l^{(d,\ell)}) \Phi_{s'}(A_r^{(d,\ell)}) dB_{A,d}(\ell) \quad (52)$$

*if  $A$  is not atomic and  $\Phi_s(A) = 1$  if  $A$  is atomic.*

## F Proof of Theorems MT-2.1 and E.1

Theorem MT-2.1 is a special case of Theorem E.1 and hence will be proven using the following proof of Theorem E.1.

*Proof.* For notational simplicity, let  $T = T^{(k)}$ . This proof will be a slight modification of the proof of Theorem 2 in Li & Ma (2021). The key difference lies in what is meant by an atom, which we define as any measurable subset of  $\Omega$  that contains exactly one training location. Under this definition, if  $A$  is atomic, then  $\Phi_s(A) = P(\mathbf{y}(A)|A \in T, S(A_p) = s) = 1$ . Now, for a node  $A$ , suppose we have shown that  $\Phi_s(B) = P(\mathbf{y}(B)|B \in T, S(B_p) = s)$  for all possible descendants  $B$  of  $A$ . If  $A$  is at depth  $j$ , it follows that

$$\begin{aligned} & P(\mathbf{y}(A)|A \in T, S(A_p) = s) \\ &= \sum_{s'} \sum_{d \in D(A)} \int_{\ell} P(\mathbf{y}(A)|A \in T, S(A) = s', S(A_p) = s, D(A) = d, L(A) = \ell) \\ & \quad \times \underbrace{P(S(A) = s'|A \in T, S(A_p) = s)}_{=: \rho_j(s, s')} \times \underbrace{P(D(A) = d|A \in T, S(A_p) = s)}_{=: \lambda_d(A)} \times dB_{A,d}(\ell) \\ &= \sum_{s'} \rho_j(s, s') \sum_d \lambda_d(A) \int_{\ell} M_{d,\ell}^{(s')}(A) \Phi_{s'}(A_l^{(d,\ell)}) \Phi_{s'}(A_r^{(d,\ell)}) dB_{A,d}(\ell), \end{aligned}$$

which leads to the definition of  $\Phi_s(A)$  in Theorem E.1.

The remainder of the proof follows by modifying the proof of Theorem 2 in Li & Ma (2021) by appropriately including split-location probabilities in the relevant places in the proof.

Now we prove the claim (49). We have

$$\begin{aligned} & P(S(A) = s', D(A) = d, L(A) = \ell, \mathbf{y}(A) | S(A_p) = s, T) \\ &= \underbrace{P(S(A) = s', D(A) = d, L(A) = \ell | S(A_p) = s, T)}_{= \rho_j(s, s') \lambda_d(A) B_{A,d}(\ell)} \\ & \quad \times \underbrace{P(\mathbf{y}(A) | S(A_p) = s, T, S(A) = s', D(A) = d, L(A) = \ell)}_{= M_{d,\ell}^{(s')}(A) \Phi_{s'}(A_l^{(d,\ell)}) \Phi_{s'}(A_r^{(d,\ell)})}. \end{aligned}$$

Marginalizing the above over  $d, \ell$ , we get

$$P(S(A) = s', \mathbf{y}(A) | S(A_p) = s, T) = \rho_j(s, s') \sum_{d \in D(A)} \lambda_d(A) \int_0^1 M_{d,\ell}^{(s')}(A) \Phi_{s'}(A_l^{(d,\ell)}) \Phi_{s'}(A_r^{(d,\ell)}) dB_{A,d}(\ell).$$

From this and the identity

$$P(S(A) = s' | S(A_p) = s, T, \mathbf{y}) = \frac{P(S(A) = s', \mathbf{y}(A) | S(A_p) = s, T)}{P(\mathbf{y}(A) | S(A_p) = s, T)}$$

where the denominator is just  $\Phi_s(A)$ , we get the claim (49).

Finally, we prove the remaining claims (50) and (51). We have

$$\begin{aligned} P(D(A) = d, L(A) = \ell | S(A) = s', T, \mathbf{y}) &= \frac{P(D(A) = d, L(A) = \ell, \mathbf{y}(A) | S(A) = s', T)}{P(\mathbf{y}(A) | S(A) = s', T)} \\ &\propto \lambda_d(A) B_{A,d}(\ell) M_{d,\ell}^{(s')}(A) \Phi_{s'}(A_l^{(d,\ell)}) \Phi_{s'}(A_r^{(d,\ell)}). \end{aligned}$$

(50) follows by marginalizing the above over  $\ell$ . (51) follows from

$$\begin{aligned} P(L(A) = \ell \mid D(A) = d, S(A) = s', T, \mathbf{y}) &= \frac{P(D(A) = d, L(A) = \ell \mid S(A) = s', T, \mathbf{y})}{P(D(A) = d \mid S(A) = s', T, \mathbf{y})} \\ &\propto B_{A,d}(\ell) M_{d,\ell}^{(s')}(A) \Phi_{s'}(A_l^{(d,\ell)}) \Phi_{s'}(A_r^{(d,\ell)}). \end{aligned}$$

□

## G Proofs for Function Reconstruction

### G.1 Euclidean

The following theorem provides an exact reconstruction of the original noisy image. To construct the estimated image, we replace the unregularized wavelet coefficients  $w_{d_i, \ell(A_i)}(A_i)$  in (53) by the regularized versions.

**Theorem G.1.** *Given a collection  $\{\mathbf{x}_i, y(\mathbf{x}_i)\}_{i=1}^n, \mathbf{x}_i \in \Omega$  with  $n > 1$  and  $y(\mathbf{x}_i) \in [0, 1]$ , let  $M_\Omega$  be the mean of all observed values  $y(\mathbf{x}_i)$  in the domain  $\Omega$ , and let  $L$  be the depth of the tree that characterizes the unbalanced splits. Given a UHWT, suppose  $A_0, A_1, \dots, A_S$  is the decreasing sequence of nodes that contain atom  $\mathbf{x}$ , where  $S \leq L - 1$ . For each  $i = 0, 1, \dots, S$ , let  $d_i$  be the axis along which node  $A_i$  is split, and let  $u_i$  be  $-1$  if  $\mathbf{x}$  is in the right child of the  $i$ th split, and  $1$  if  $\mathbf{x}$  is in the left child of the  $i$ th split. Then  $y(\mathbf{x})$  equals*

$$M_\Omega + \sum_{i=0}^{S-1} u_i \frac{w_{d_i, \ell(A_i)}(A_i)}{c(A_i)} \text{ where } c(A_i) = |A_i|^{1/2} \left( \frac{|A_{i,l}^{(d_i)}|}{|A_{i,r}^{(d_i)}|} \right)^{u_i/2}, \quad (53)$$

where  $w_{d_i, \ell(A_i)}$  is the UH coefficient (MT-3) for the partition component for the node  $A_i$ .

*Proof.* For any node  $A$ , let  $\overline{y(A)} := |A|^{-1} \sum_{\mathbf{x} \in A} y(\mathbf{x})$  be the mean of all pixel values in  $A$ . For all  $k = 0, 1, \dots, S$ , define

$$Q_k := \overline{y(A_k)} + \sum_{i=k}^{S-1} u_i \frac{w_{d_i, \ell(A_i)}(A_i)}{c(A_i)}.$$

(Here a summation vanishes if its starting index is larger than its ending index.) Because  $Q_0$  equals (53) and  $Q_S = \overline{y(A_S)} = y(\mathbf{x})$ , it suffices to show that  $Q_0 = Q_1 = \dots = Q_S$ .

For all  $k = 0, 1, \dots, (S-1)$ , we have  $\overline{y(A_k)} = \frac{1}{|A_k|} \sum_{\mathbf{a} \in A_{k,l}^{(d_k)}} y(\mathbf{a}) + \frac{1}{|A_k|} \sum_{\mathbf{a} \in A_{k,r}^{(d_k)}} y(\mathbf{a})$  and

$$\begin{aligned} \overline{y(A_k)} + \ell_k \frac{w_{d_k}^{\text{UH}}(A_k)}{c(A_k)} &= \left[ \frac{1}{|A_k|} + \ell_k \frac{1}{c(A_k)} \left( \frac{1}{|A_{k,l}^{(d_k)}|} - \frac{1}{|A_k|} \right)^{1/2} \right] \sum_{\mathbf{a} \in A_{k,l}^{(d_k)}} y(\mathbf{a}) \\ &\quad + \left[ \frac{1}{|A_k|} - \ell_k \frac{1}{c(A_k)} \left( \frac{1}{|A_{k,r}^{(d_k)}|} - \frac{1}{|A_k|} \right)^{1/2} \right] \sum_{\mathbf{a} \in A_{k,r}^{(d_k)}} y(\mathbf{a}) \\ &= \begin{cases} \overline{y(A_{k,l}^{(d_k)})} & \text{if } \ell_k = 1 \\ \overline{y(A_{k,r}^{(d_k)})} & \text{if } \ell_k = -1 \end{cases} \\ &= \overline{y(A_{k+1})} \end{aligned}$$

By adding the term  $\sum_{i=k+1}^{S-1} u_i \frac{w_{d_i, \ell(A_i)}(A_i)}{c(A_i)}$  to every line in the preceding panel, we get  $Q_k = Q_{k+1}$ , which implies  $Q_0 = Q_1 = \dots = Q_S$ .  $\square$

## G.2 General domain

Theorem G.2 below extends Theorem G.1 to 1-4 splits and to a more general domain that has a notion of “area” or “volume.” Such a domain might not have a natural notion of which child is the “left” or “right” one, particularly if there is no natural coordinate axis. Here we provide a labeling for such a case. (The end of this subsection shows that this labeling is valid even though it does not depend on any intrinsic properties of the nodes and is chosen entirely by the user.)

Define the *signed indicator*:

$$\ell_j = \begin{cases} +1, & \text{if } x \in A_{j,\ell} \text{ (in a 1-2 split)} \\ -1, & \text{if } x \in A_{j,r} \end{cases} \quad \text{or} \quad \ell_j = \begin{cases} +1, & \text{if } x \in \{A_{j,0}, A_{j,2}\} \text{ (in a 1-4 split)} \\ -1, & \text{if } x \in \{A_{j,1}, A_{j,3}\} \end{cases} \quad (54)$$

A 1-2 split we label the two children

$$A_\ell \quad (\text{the positive half-plane}), \quad A_r \quad (\text{the negative one}). \quad (55)$$

A 1-4 split still has one parent  $A$  but now four grandchildren:

$$A_0, A_1, A_2, A_3. \quad (56)$$

To preserve the orthogonality of the UH wavelets, we *group* those four grandchildren into two aggregate halves:

$$A^+ = A_0 \cup A_2, \quad A^- = A_1 \cup A_3. \quad (57)$$

Everything that was “left vs right” in the 1-2 split becomes “ $A^+$  vs  $A^-$ ” in the 1-4 split.

$$\bullet \quad \bar{y}_{A_\ell} \longrightarrow \bar{y}_{A^+} = \frac{|A_0|\bar{y}_{A_0} + |A_2|\bar{y}_{A_2}}{|A^+|}$$

- $\bar{y}_{A_r} \longrightarrow \bar{y}_{A^-} = \frac{|A_1|\bar{y}_{A_1} + |A_3|\bar{y}_{A_3}}{|A^-|}$
- $|A_\ell| \longrightarrow |A^+| = |A_0| + |A_2|$
- $|A_r| \longrightarrow |A^-| = |A_1| + |A_3|$
- $\ell_j = \begin{cases} +1 & \text{if } x \in \{A_0, A_2\} \\ -1 & \text{if } x \in \{A_1, A_3\} \end{cases}$

**Theorem G.2.** Suppose we have a training collection  $\{\mathbf{x}_a, y(\mathbf{x}_a)\}_{a=1}^n, \mathbf{x}_a \in \Omega$  with  $n > 1$  and  $y(\mathbf{x}_a) \in \mathbb{R}$ . For any node  $A$ , define  $y(A) := \sum_{\mathbf{x}_a \in A} y(\mathbf{x}_a)$ , i.e.,  $y(A)$  is the sum of all training response values whose locations are in  $A$ . Given a UHWT, for any node  $A$  in the UHWT with child sets  $A^+$  and  $A^-$  also in the UHWT, let

$$w(A) = \sqrt{\frac{|A^+| \cdot |A^-|}{|A|}} [y(A^+) - y(A^-)] \quad (58)$$

where  $|A| = |A|_n$  denotes the number of training points in node  $A$ . Given a location  $\mathbf{x}^* \in \{\mathbf{x}_i\}_{i=1}^n$ , suppose the UHWT has a node  $A_S$  at depth  $S$  that contains  $\mathbf{x}^*$  and no other training location, and thus let  $A_S, A_{S-1}, \dots, A_1, A_0$  be the telescoping sequence of nodes along the UHWT tree, where  $A_0 = \Omega$ . For each  $i = 0, 1, \dots, S$ , let  $u_i$  be  $-1$  if  $\mathbf{x}^*$  is in the “minus” child set  $A_i^-$  of the  $i$ th split, and  $1$  if  $\mathbf{x}^*$  is in the “plus” child set  $A_i^+$  of the  $i$ th split. For all  $k = 0, 1, \dots, S$ , define

$$Q_k := \frac{y(A_k)}{|A_k|} + \sum_{i=k}^{S-1} u_i \frac{w(A_i)}{c(A_i)}, \text{ where } c(A_i) = |A_i|^{1/2} \left( \frac{|A_i^+|}{|A_i^-|} \right)^{u_i/2}.$$

Then  $y(\mathbf{x}^*) = Q_0 = Q_1 = \dots = Q_S$ .

*Proof.* Because  $Q_S = \frac{y(A_S)}{|A_S|} = y(\mathbf{x}^*)$ , it suffices to show that  $Q_0 = Q_1 = \dots = Q_S$ .

For any  $i = 0, 1, \dots, S-1$ , we have

$$\frac{w(A_i)}{c(A_i)} = \frac{1}{|A_i|} \left( \frac{|A_i^-|}{|A_i^+|} \right)^{u_i/2} \left[ \left( \frac{|A_i^-|}{|A_i^+|} \right)^{1/2} y(A_i^+) - \left( \frac{|A_i^+|}{|A_i^-|} \right)^{1/2} y(A_i^-) \right].$$

For all  $k = 0, 1, \dots, (S-1)$ , we have  $y(A_k) = y(A_k^+) + y(A_k^-)$  and thus

$$\begin{aligned} \frac{y(A_i)}{|A_i|} + u_i \frac{w(A_i)}{c(A_i)} &= \frac{1}{|A_i|} \left[ 1 + u_i \left( \frac{|A_i^-|}{|A_i^+|} \right)^{(1+u_i)/2} \right] y(A_i^+) \\ &\quad + \frac{1}{|A_i|} \left[ 1 - u_i \left( \frac{|A_i^+|}{|A_i^-|} \right)^{(1-u_i)/2} \right] y(A_i^-) \\ &= \begin{cases} y(A_i^+)/|A_i^+| & \text{if } u_i = 1 \\ y(A_i^-)/|A_i^-| & \text{if } u_i = -1 \end{cases} \\ &= \frac{y(A_{i+1})}{|A_{i+1}|}. \end{aligned}$$

In this panel, the left-most term minus the right-most term equals  $Q_i - Q_{i+1}$ . Thus we get  $Q_i = Q_{i+1}$ . Because this holds for all  $i$ , we get  $Q_0 = Q_1 = \dots = Q_S$ .  $\square$

We remark that the "plus" and "minus" labeling of children does not depend on any intrinsic properties of the nodes and is chosen entirely by the user. We prove this here. Given the telescoping sequence  $A_S, \dots, A_1, A_0$  from the previous theorem, let  $B_k = A_k$  for all  $k$ , but suppose we swap the plus and minus labels of the children of the node  $B_j$  at some depth  $j = 0, 1, \dots, S-1$  so that  $A_j^+ = B_j^-$  and  $A_j^- = B_j^+$ , but  $A_k^+ = B_k^+$  and  $A_k^- = B_k^-$  and for all  $k \neq j$ . We then would have  $\ell_j^A = -\ell_j^B$ , but  $\ell_k^A = \ell_k^B$  for all  $k \neq j$ . Comparing  $\{Q_k^B\}_{k=0}^S$  to  $\{Q_k^A\}_{k=0}^S$ , we note that any difference could only stem from a difference between

$$\ell_j^B \frac{w(B_j)}{c(B_j)} \quad \text{vs} \quad \ell_j^A \frac{w(A_j)}{c(A_j)}. \quad (59)$$

But we have

$$c(B_j) = |B_j|^{1/2} \left( \frac{|B_j^+|}{|B_j^-|} \right)^{\ell_j^B/2} = |A_j|^{1/2} \left( \frac{|A_j^-|}{|A_j^+|} \right)^{(-\ell_j^A)/2} = c(A_j)$$

and

$$\begin{aligned} \ell_j^B w(B_j) &= \ell_j^B \sqrt{\frac{|B_j^+| \cdot |B_j^-|}{|B_j|}} [y(B_j^+) - y(B_j^-)] = (-\ell_j^A) \sqrt{\frac{|A_j^-| \cdot |A_j^+|}{|A_j|}} [y(A_j^-) - y(A_j^+)] \\ &= \ell_j^A w(A_j). \end{aligned}$$

Thus the two terms in (59) are equal to each other, and so  $Q_k^B = Q_k^A$  for all  $k$ .

### G.3 Connection to SHAH Algorithm

Our proposed UHWT algorithm has a connection to the SHAH algorithm from [Fryzlewicz & Timmermans \(2016\)](#). The SHAH algorithm takes a bottom-up approach that merges the two neighboring pixel pairs with the minimum absolute value of detailed coefficients, which has the same complexity as single linkage hierarchical clustering of  $O(n^2)$ , slower than our Algorithm 1's additional  $O(D \cdot L \cdot n/2^L)$  complexity if  $L$  grows with  $n$  (Also see Section J).

To see this connection, suppose the SHAH algorithm merges two nodes  $j$  and  $k$  (not necessarily atoms), where their respective squared weights  $w_j^2$  and  $w_k^2$  equal the number of cells in the respective nodes  $j$  and  $k$ . Then the merged node by definition has squared weight equal to  $w_j^2 + w_k^2$ , which by assumption equals the sum of the number of cells in the two nodes  $j$  and  $k$ . By definition of SHAH algorithm, the merged node (which we index as node  $\ell$ ) has term

$$X_\ell := \frac{w_j X_j + w_k X_k}{\sqrt{w_j^2 + w_k^2}}.$$

then  $w_j X_j$  equals the sum of the pixel values in node  $j$ , and  $w_k X_k$  equals the sum of the pixel values in node  $k$ . Thus the numerator in the above panel equals the sum of the pixel

values in the merged node. Furthermore, the denominator equals the square root of number of atoms in the merged node.

Suppose any atom has weight equal to 1 and is an atomic node, the detailed coefficient

$$\tilde{d}_\ell := \frac{w_j}{\sqrt{w_j^2 + w_k^2}} X_k - \frac{w_k}{\sqrt{w_j^2 + w_k^2}} X_j = \frac{1}{\sqrt{n_\ell}} \left( \frac{\sqrt{n_j}}{\sqrt{n_k}} \sum_{\text{atom } i \text{ in node } k} y_i - \frac{\sqrt{n_k}}{\sqrt{n_j}} \sum_{\text{atom } i \text{ in node } j} y_i \right),$$

which is exactly  $w_{d,\ell}(A)$  in (MT-3). By the SHAH algorithm, two neighboring nodes are chosen to merge if the edge between them has the minimum absolute value of detail among any pair of neighboring nodes. This is equivalent to splitting a node at the location with the maximum absolute value of detail. Therefore, our algorithm can be considered a generalization of SHAH.

## H Proof of Theorem MT-5.1

*Proof.* Since  $\mu = \mu_n$  on the grid,  $\{\psi_j\}$  is orthonormal in  $L^2(\mu)$  and  $w_j = \theta_j + z_j$  with  $\theta_j = \langle f, \psi_j \rangle$  and  $z_j = \langle \varepsilon, \psi_j \rangle$  sub-Gaussian with proxy  $\sigma/\sqrt{n}$ . A union bound gives  $\max_j |z_j| \leq \tau$  with probability at least  $1 - \delta$ . On this event, the standard orthogonal soft-thresholding argument in Lemma H.1 yields, for any  $S \subset \{1, \dots, M\}$ , the inequality

$$\sum_{j=1}^M \left( \operatorname{sgn}(w_j)(|w_j| - \tau)_+ - \theta_j \right)^2 \leq 4 \sum_{j \notin S} \theta_j^2 + 4|S|\tau^2. \quad (60)$$

Adding the constant component and using orthonormality in  $L^2(\mu)$  gives the UH-estimator inequality (MT-26). For the leafwise inequality (MT-27), for each  $A \in \mathcal{P}$  we define

$$\bar{f}_A := \frac{1}{N_A} \sum_{i: \mathbf{X}_i \in A} f(\mathbf{X}_i) \quad \text{and} \quad \bar{\varepsilon}_A := \frac{1}{N_A} \sum_{i: \mathbf{X}_i \in A} \varepsilon_i,$$

decompose  $\hat{f}_{\mathcal{P}}^{\text{leaf}} - f$  on  $A$  as  $(\bar{f}_A - f) + \bar{\varepsilon}_A$ , and union-bound control  $\bar{\varepsilon}_A$  to yield the stated variance term. The Hölder bound on  $\|f - f_{\mathcal{P}}\|$  is standard.

In both the grid construction and the triangulated construction, the paper proves that each admissible split produces two child indicator functions which are balanced and normalized with respect to the current measure. This guarantees orthogonality of the new detail to the space generated so far, and it also guarantees unit norm in  $L_2(\nu)$ . Since every split raises the number of cells by one, after  $|\mathcal{P}| - |\mathcal{P}_0|$  splits we have exactly  $|\mathcal{P}| - |\mathcal{P}_0|$  such details. The reconstruction identities given in the paper for the grid case and for the triangulated case show that these details together with the global mean span the whole space of piecewise-constant functions on the final partition. Once this orthonormal system is available, the coefficientwise soft-thresholding argument of the paper applies without change in either domain and yields the oracle inequality with  $M = |\mathcal{P}| - |\mathcal{P}_0|$ . The proof of the leafwise bound is also independent of the domain since it only uses the union bound for the empirical noise means on each cell of the same partition.  $\square$

**Lemma H.1** (Soft-thresholding inequality). *Let  $\theta = (\theta_j)_{j=1}^M \in \mathbb{R}^M$ . Suppose for some  $\tau > 0$  that  $z = (z_j)_{j=1}^M \in \mathbb{R}^M$  satisfies the coordinatewise bound*

$$\|z\|_\infty := \max_{1 \leq j \leq M} |z_j| \leq \tau. \quad (61)$$

*Define the soft-threshold map  $\eta_\tau(y) = \text{sign}(y) (|y| - \tau)_+$ . Define  $\hat{\theta} = (\hat{\theta}_j)_{j=1}^M$  by soft-thresholding the noisy coefficients  $\theta + z$ :*

$$\hat{\theta}_j = \eta_\tau(\theta_j + z_j) \quad (j = 1, \dots, M). \quad (62)$$

*Then the following deterministic inequalities hold:*

$$\sum_{j=1}^M (\hat{\theta}_j - \theta_j)^2 \leq 4 \sum_{j=1}^M \min \{ \theta_j^2, \tau^2 \}, \quad (63)$$

$$\leq 4 \left( \sum_{j \notin S} \theta_j^2 + |S| \tau^2 \right) \quad \text{for every subset } S \subset \{1, \dots, M\}. \quad (64)$$

*Proof.* We prove (63) by a coordinatewise argument, then sum over  $j$ ; (64) is an immediate consequence.

Fix an index  $j$  and set

$$a = \theta_j, \quad b = z_j, \quad u = a + b, \quad \hat{a} = \eta_\tau(u). \quad (65)$$

Our goal is to show the scalar inequality

$$(\hat{a} - a)^2 \leq 4 \min \{ a^2, \tau^2 \} \quad \text{under the bound } |b| \leq \tau. \quad (66)$$

Summing (66) over  $j$  yields (63).

We consider two disjoint cases:

*Case 1:*  $|u| \leq \tau$ . By the triangle inequality,

$$|a| \leq |u| + |b| \leq \tau + \tau = 2\tau, \quad (67)$$

hence  $a^2 \leq 4\tau^2$ . Because the inequality  $|u| \leq \tau$  implies  $\hat{a} = \eta_\tau(u) = 0$ , we get

$$(\hat{a} - a)^2 = (0 - a)^2 = a^2 \leq \min \{ a^2, 4\tau^2 \} \leq 4 \min \{ a^2, \tau^2 \}. \quad (68)$$

*Case 2:*  $|u| > \tau$ . Then  $\hat{a} = \eta_\tau(u) = u - \tau \text{sign}(u)$  and

$$\hat{a} - a = \{u - \tau \text{sign}(u)\} - a = b - \tau \text{sign}(u). \quad (69)$$

We split Case 2 into two subcases.

*Case 2a:*  $|a| \geq \tau$ . Then  $\min \{ a^2, \tau^2 \} = \tau^2$ . From (69) and the triangle inequality,

$$|\hat{a} - a| = |b - \tau \text{sign}(u)| \leq |b| + \tau \leq \tau + \tau = 2\tau. \quad (70)$$

Hence

$$(\hat{a} - a)^2 \leq 4\tau^2 = 4\min\{a^2, \tau^2\}. \quad (71)$$

Case 2b:  $|a| < \tau$ . Then  $\min\{a^2, \tau^2\} = a^2$ . Using (69), the triangle inequality, and the identity  $|\eta_\tau(u)| = |u| - \tau$  (which holds because  $|u| > \tau$  by assumption), we obtain

$$|\hat{a} - a| \leq |\hat{a}| + |a| = (|u| - \tau) + |a| \quad (72)$$

$$\leq (|a| + |b| - \tau) + |a| \quad (\text{by } |u| = |a + b| \leq |a| + |b|) \quad (73)$$

$$\leq |a| + |a| = 2|a| \quad (\text{since } |b| \leq \tau) \quad (74)$$

and therefore

$$(\hat{a} - a)^2 \leq 4a^2 = 4\min\{a^2, \tau^2\}. \quad (75)$$

In Case 1 we have (68). In Case 2a we have (71). In Case 2b we have (75). These three inequalities exhaust all possibilities for  $(a, b)$  under  $|b| \leq \tau$  and each yields (66). Summing the scalar bound over  $j = 1, \dots, M$  gives (63).

Fix an arbitrary subset  $S \subset \{1, \dots, M\}$ . For each  $j$ ,

$$\min\{\theta_j^2, \tau^2\} \leq \begin{cases} \tau^2, & j \in S, \\ \theta_j^2, & j \notin S. \end{cases} \quad (76)$$

Combine with (63) to obtain (64).  $\square$

## I Proof of Corollary MT-5.2

*Proof.* By Theorem MT-5.1, for  $\tau = \sigma\sqrt{2n^{-1}\log(2M/\delta)}$  the UH soft-thresholded estimator satisfies, with probability at least  $1 - \delta$ ,

$$\|\hat{f}_{P,\tau}^{\text{UH}} - f\|_{L^2(\mu)}^2 \leq 4 \inf_{S \subset \{1, \dots, M\}} \left\{ \|f - f_S\|_{L^2(\mu)}^2 + 2|S| \frac{\sigma^2}{n} \log \frac{2M}{\delta} \right\}. \quad (77)$$

Taking  $S = S^*$  and using the assumption  $f = f_{S^*}$  yields

$$\|\hat{f}_{P,\tau}^{\text{UH}} - f\|_{L^2(\mu)}^2 \leq 8s \frac{\sigma^2}{n} \log \frac{2M}{\delta}. \quad (78)$$

For the leafwise estimator, Theorem MT-5.1 gives, with probability at least  $1 - \delta$ ,

$$\|\hat{f}_{\mathcal{P}}^{\text{leaf}} - f\|_{L^2(\mu)}^2 \leq \|f - f_{\mathcal{P}}\|_{L^2(\mu)}^2 + 4 \frac{\sigma^2}{m_{\min}(\mathcal{P})} \log \frac{2|\mathcal{P}|}{\delta}. \quad (79)$$

Since  $f$  is piecewise-constant on  $\mathcal{P}$  by assumption ( $f \in \text{span}\{1, \psi_j\}_{j \in S^*}$ ), we have  $f = f_{\mathcal{P}}$  and the approximation term vanishes. The  $c$ -balance condition  $m_{\min}(\mathcal{P}) \geq cn/|\mathcal{P}|$  implies

$$\|\hat{f}_{\mathcal{P}}^{\text{leaf}} - f\|_{L^2(\mu)}^2 \leq \frac{4}{c} |\mathcal{P}| \frac{\sigma^2}{n} \log \frac{2|\mathcal{P}|}{\delta}. \quad (80)$$

This proves the two bounds and the stated comparison of variance scales.  $\square$

## J Complexity

We use the following notations in this section:

- $n$ : number of observations,  $\mathbf{x}_i \in \mathbb{R}^D$ , all assumed unit-norm.
- $D$ : embedding dimension ( $D = 3$  for the sphere).
- $L$ : maximal tree depth; with regular refinement  $L = \lceil \log_2 n \rceil$ .
- $n_\ell$ : total number of points stored in depth  $\ell$  of a tree.
- $M$ : number of trees in an ensemble.

For every method we give *time*  $T(\cdot)$  and *space*  $S(\cdot)$  in big- $O$  / big- $\Theta$  form and lower-order constants are omitted.

Method	Time $T(n, D)$	Space $S(n)$
single-tree <b>balance</b> or <b>balance4</b>	$\Theta(D nL)$	$\Theta(n)$
single-tree <b>adapt</b> or <b>adapt_vertex</b>	$\Theta(D n^2)$	$\Theta(n)$
Random Rotation Forest ( <b>balance</b> )	$M(O(D^3) + O(nD^2) + \Theta(D nL))$	$\Theta(Mn)$
Random Rotation Forest ( <b>adapt</b> )	$M(O(D^3) + O(nD^2) + \Theta(D n^2))$	$\Theta(Mn)$
Rotation Forest (Euclidean PCA)	$M(O(bD^3/K^2) + \Theta(D nL))$	$\Theta(Mn)$
SPCA Rotation Forest	$M(O(n) + \Theta(D nL))$	$\Theta(Mn)$
Gaussian Process on $\mathbb{S}^{D-1}$	$\Theta(n^3)$	$\Theta(n^2)$

Table 4: Asymptotic training complexity (See SM J for detailed derivations).  $L = \lceil \log_2 n \rceil$ ,  $M$  = ensemble size,  $b$  the bootstrap fraction and  $K$  the block count in Euclidean Rotation Forest. For  $D = 3$  the terms  $O(D^3)$  and  $O(nD^2)$  are constant-factor overheads.

### J.1 Single-tree splitters

**Balanced midpoint split (method **balance**).** The procedure satisfies

$$T_{\text{bal}}(n, D) = \Theta(D nL), \quad S_{\text{bal}}(n) = \Theta(n). \quad (81)$$

At any node containing  $n_\ell$  points one performs the

1. longest-edge search:  $O(1)$  arithmetic,
2. one midpoint evaluation:  $O(D)$ ,
3. a single membership scan of the local list:  $O(D n_\ell)$ .

Because the lists of siblings form a partition of the parent list we have  $\sum_{\ell=0}^L n_\ell = n$ . Summation over depths therefore yields  $DnL$ . Each sample index is stored exactly once, hence linear memory.

**Balanced four-way split (method **balance4**).** In the worst case

$$T_{\text{bal4}}(n, D) = \Theta(D nL), \quad S_{\text{bal4}}(n) = \Theta(n). \quad (82)$$

Every point is still inspected once per tree level; the factor 4 in the number of children changes only the leading constant.

**Adaptive edge split (methods `adapt` and `adapt_vertex`).** In the worst case

$$T_{\text{adapt}}(n, D) = T_{\text{adapt\_vertex}}(n, D) = \Theta(D n^2), \quad S_{\text{adapt}}(n) = \Theta(n). \quad (83)$$

Inside a node with  $n_\ell$  points, the algorithm selects *every* point as pivot and, for each of three edges, rescans the full list. Cost per node =  $O(3D n_\ell^2)$ . If early splits are rejected the root remains with  $n_\ell = n$ , giving  $Dn^2$ . Memory is unchanged.

## J.2 Rotation ensembles

All ensembles apply a pointwise rotation  $\mathbf{x} \mapsto \mathbf{x}R^\top$  before calling a base splitter; prediction averages  $M$  trees and costs  $O(Mn)$ .

**Random-Rotation Ensemble (RRE).** In each tree:

1. sample  $R \in SO(D)$  via QR:  $O(D^3)$ ,
2. rotate data:  $O(nD^2)$ ,
3. build a tree:  $T_{\text{tree}}(n, D)$ .

Hence

$$T_{\text{RRE}}(n, D, M) = M(O(D^3) + O(nD^2) + T_{\text{tree}}(n, D)). \quad (84)$$

For  $D = 3$  the algebraic overhead is constant.

**Rotation Forest (Euclidean PCA).** Let  $K$  be the block count and  $b \in (0, 1]$  the bootstrap fraction. Per tree one performs  $K$  SVDs of size  $bn \times D/K$ , each  $O((D/K)^3)$ . Thus

$$T_{\text{RotF}} = M(O(bD^3/K^2) + T_{\text{tree}}(n, D)), \quad (85)$$

again constant for  $D = 3$ .

**Rotation Forest with spherical PCA (sPCA, [Luo et al. \(2024\)](#)).** Principal geodesic analysis in  $\mathbb{R}^3$  costs  $O(bnD) + O(D^3) = O(n)$  per tree (dominated by mean and projection). Therefore

$$T_{\text{sPCA-RotF}}(n, 3, M) = M T_{\text{tree}}(n, 3) + O(M). \quad (86)$$

## J.3 Intrinsic Gaussian process on the sphere

Exact GP regression with a Matérn kernel on the sphere  $\mathbb{S}^2$  satisfies

$$T_{\text{GP}}(n) = \Theta(n^3), \quad S_{\text{GP}}(n) = \Theta(n^2), \quad (87)$$

and prediction at  $m$  new points costs  $\Theta(mn)$ .

*Proof.* Optimization of the exact marginal likelihood requires one inversion or Cholesky factorisation of the  $n \times n$  covariance matrix; both are cubic. The dense matrix itself stores  $n^2$  entries. Posterior mean evaluation multiplies the same matrix inverse by  $m$  right-hand sides.  $\square$

## K Other tree-based methods for manifold domains

Other tree-based methods for manifold domains, such as BAST (Luo et al. 2021) and BAMDT (Luo et al. 2022), build adaptive partitions by cutting along a spanning tree in a neighborhood graph rather than by refining faces of a triangulation. Medoid trees (Bulté & Sørensen 2024) partition observations directly to reduce within node dispersion, but they do not introduce nested simplicial refinements. In contrast, our UHWT refines within faces when needed. This allows it to emulate the flexible random partitions of spanning tree methods while maintaining a sample exact reconstruction and a multiscale representation that follows edges on curved surfaces. More global approaches based on graph spectral wavelets (Mostowsky et al. 2024) or diffusion frames (Hui et al. 2022) rely on eigen-decompositions of a Laplace operator and do not yield a recursive data driven partition. Mesh-based wavelets such as those of Schröder & Sweldens (1995) assume a fixed nested tessellation and so cannot adapt to sparse or irregular sampling, which our data-driven partitions can handle relatively well even with shallow trees.

## L Further numerical experiments

### L.1 Comparison to other image denoising methods

Here we provide numerical comparisons of our wavelet-based methods and general-use tree ensemble methods. These comparisons will use real-world images. In both applications, we will see that our boosting wavelet approach, which utilizes both wavelet technology and ensembling, often has superior MSE performance against the tested methods. We will see that many existing wavelet approaches are not able to overcome the benefit gained by ensembling single learners, and that general-use tree ensembles cannot overcome the benefits of wavelet-specific approaches (e.g., energy conservation, sharp-edge detection) that have been massively developed in image processing.

#### L.1.1 OCT

For the first set of comparisons, we use optical coherence tomography (OCT) image slices available at [https://people.duke.edu/~sf59/fang\\_tmi\\_2013.htm](https://people.duke.edu/~sf59/fang_tmi_2013.htm). For each of the 18 slices, there is an image with noise already included and a registered image obtained by averaging 40 repeatedly sampled scans (Fang et al. 2016); we use the latter as the “noiseless” reference image to compare our denoised images against. Due to WARP requiring image size dimensions to be powers of two, we resize these images from  $900 \times 450$  to  $1024 \times 512$ .

On these images, we fit models using our boosting approach and our backfitting approach with each tree grown using Metropolis-Hastings and either the Laplace or spike-and-slab likelihood. For boosting we use 500 estimators and learning rate 0.05; we also explore various pruning values. For our backfitting approach we use 200 estimators and 70 backfitting iterations and prior node-split probability  $0.95 * 0.5^{\text{depth}}$ . We compare our approaches against WARP with cycle spinning (BMA) (Li & Ma 2021, Li & Ghosal 2015), SHAH (Fryzlewicz & Timmermans 2016), Translation-invariant (TI) de-noising (Coifman & Donoho 1995), Bayesian Additive Regression Trees (Chipman et al. 2010) using the BART R package in CRAN (Sparapani et al. 2021), and nonparametric Bayesian dictionary learning (Zhou

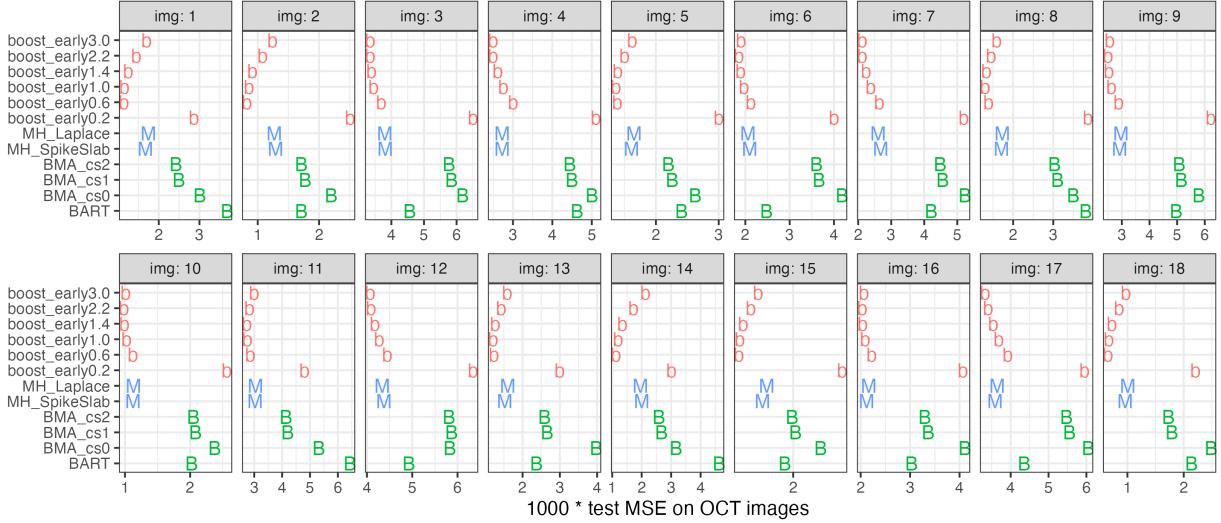


Figure 7: Test MSE on 18 OCT images. boost denotes forward stagewise boosting with the stated prune parameter  $b$  used in the data-independent thresholding quantity  $\tau = b\sqrt{2 \log n}$  as described in Section MT-2.2. MH\_Laplace and MH\_SpikeSlab denote the posterior mean of the backfitting-ensemble draws with each tree grown using Metropolis-Hastings and either the Laplace or spike-and-slab likelihood, respectively. BMA denotes WARP with the stated step size for cycle spinning (cs).

et al. 2011). Cycle spinning is a technique that can be used to remove visual artifacts when reconstructing an image.

Figure 7 shows the test MSE of the denoised images using boosting with various pruning thresholds, our backfitting approach, BMA with various cycle-spinning steps, and BART. For each image, we found SHAH and TI to produce markedly larger MSEs than either boosting or BMA. Furthermore, we found that nonparametric Bayesian dictionary learning takes longer than boosting and requires 5GB cache for 18 OCT images. Hence, we show the MSE results for only boosting, MH, BMA, and BART. We find for prune parameters between 0.6 and 3.0 that boosting has smaller test MSE than does BMA or BART. It seems that increasing the amount of cycle spinning in BMA will further lower the test MSE, but not to an amount smaller than the shown boosting MSEs. Furthermore, we see that the boosting MSEs exhibit a ‘U’ shape with respect to the prune parameter, which indicates a bias-variance trade-off. Namely, the prune parameter  $b = 0.2$  provides too little regularization to prevent overfitting. Finally, we see that our backfitting approach produces test MSEs comparable to those of boosting. Generally, we find that the denoised images for boosting and BMA to be crisper than those for MH and BART, which tend to be more textured.

### L.1.2 BSDS

For this set of comparisons, we use 300 natural images from the Berkeley segmentation dataset (BSDS300). For each noiseless image, we created six noisy versions. For the first noise mechanism, we add Gaussian noise with a standard deviation equal to, respectively, 0.2, 0.4, and 0.6 times the noiseless image’s pixel-value standard deviation. For the second

noise mechanism, we add Gaussian noise with a standard deviation equal to 5/255, 10/255, and 15/255. Thus each model is ultimately trained on  $300 \times (3 + 3) = 1800$  noisy images. Due to the many training images and WARP requiring image size dimensions to be powers of two, we resize these natural images to  $256 \times 256$ .

To these images, we fit models using our boosting approach and our backfitting approach with either Laplace or spike-and-slab likelihoods. For boosting we use 500 estimators and learning rate 0.05; we also explore various pruning values. For our backfitting approach we use 1000 estimators and 500 backfitting iterations and prior node-split probability  $0.95 * 0.5^{\text{depth}}$ . We compare our approaches against BMA, BART, SHAH, and TI using the same code implementation as in Section L.1.1.

The top row of Figure 8 shows the test MSE averaged over all 300 images for each noise level when the noise level depends on the noiseless image’s standard deviation. At each noise level, the smallest test MSE is achieved by either boosting or BMA. boosting does best at the smallest noise level, but BMA overtakes boosting for the larger noise levels. However, we find that BMA tends to oversmooth textures in the noiseless images. For example, the top row of Figure 9 shows a noisy image (noise level 0.2) with visible hexagonal tiling on the ground. BMA’s denoised image omits almost any hint of the hexagons, whereas boosting is able to preserve most of the hexagons. Even when the noise level is increased to 0.4 (bottom row of Figure 9), boosting is still able to preserve a little bit of the hexagonal tiling. The general pattern we found is that boosting tends to preserve textures (e.g., ripples in a river, rock surfaces) and curved boundaries (e.g., of an owl) better than BMA does.

For the first noise mechanism, the additive noise is generated according to

$$\sigma \in \{0.2, 0.4, 0.6\} \times \text{sd}(I_i), \quad (88)$$

where  $\text{sd}(I_i)$  is the standard deviation of the  $i$ -th clean BSDS image  $I_i$ . This rule couples the magnitude of the perturbation to image content: high-contrast or highly textured images receive larger *absolute* noise than smooth images. Consequently the experiment becomes heteroskedastic across images even when the nominal “noise level” is the same. The BMA denoiser, particularly with cycle spinning, adapts its shrinkage to the noise standard deviation on a per-image basis and thereby behaves like a variance-normalized estimator. When the noise standard deviation  $\sigma_i$  increases with  $\text{sd}(I_i)$  (where  $I_i$  is the  $i$ th clean BSDS image), the risk-optimal shrinkage on rough images becomes more aggressive, which reduces the pixelwise MSE but also suppresses fine textures. Models whose hyperparameters are tuned globally across images (e.g., boosted ensembles with capacity fixed per “noise level”) cannot match this per-image adaptation and are penalized precisely on the images where the absolute noise has been inflated by design. The pattern in the top row of Figure 8—BMA overtaking at the higher reported noise levels while qualitative panels reveal oversmoothing—is consistent with this mechanism.

To eliminate the confounding, the injected noise must be decoupled from image content. Hence for our second noise mechanism, we add i.i.d. Gaussian noise with a fixed *absolute* standard deviation  $\sigma_i \in \{5, 10, 15, 20, 25, 30\}/255$  after scaling all images to  $[0, 1]$ . Hyperparameters are selected once per  $\sigma$  on a validation set of training images rather than per test image. Model capacities are matched across methods by equating effective degrees

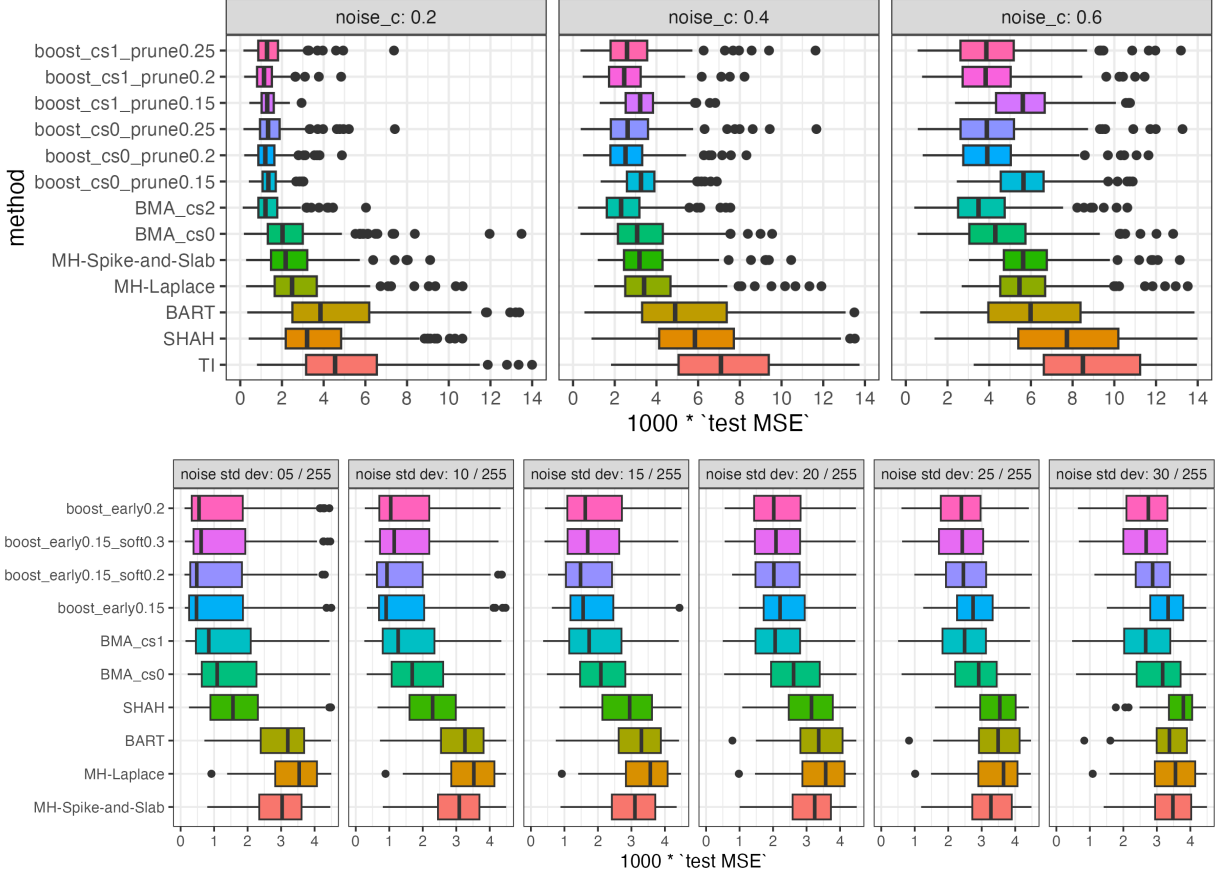


Figure 8: Test MSE times  $10^3$  averaged over 300 BSDS images. Each panel corresponds to the stated noise level (**top**: noise standard deviation is  $\text{noise\_c} \times \text{sd}(\text{image})$ ; **bottom**: noise standard deviation is as stated and is independent of  $\text{sd}(\text{image})$ ). Each row represents a method with some hyperparameter values; for the BMA columns, “cs” indicates cycle spinning with some number of steps; for the boost columns, “b” indicates hyperparameter  $b$  defined in § MT-6.1. MH-Laplace and MH-Spike-and-Slab represent the posterior mean of the backfitting-ensemble draws with each tree grown using Metropolis-Hastings and either the Laplace or spike-and-slab likelihood, respectively.

of freedom, for example by comparing a single tree with  $L$  leaves to a boosting run whose total leaves across trees are approximately  $L$ .

We re-run the study under both the original noise rule and the corrected protocol and examine the per-image difference

$$\Delta_i = \text{MSE}_{\text{BMA}}(i) - \text{MSE}_{\text{boost}}(i). \quad (89)$$

Under the original rule a simple regression  $\Delta_i = \beta_0 + \beta \text{sd}(I_i) + \epsilon_i$  should yield  $\hat{\beta} < 0$ , indicating that BMA appears better precisely when  $\text{sd}(I_i)$  is large because those images were assigned larger absolute noise. Under the corrected protocol the slope should be statistically indistinguishable from zero, and the apparent advantage of BMA on high-contrast images should diminish; as capacity increases under matched budgets the ranking between single-tree and ensemble estimators should stabilize or reverse for reasons intrinsic

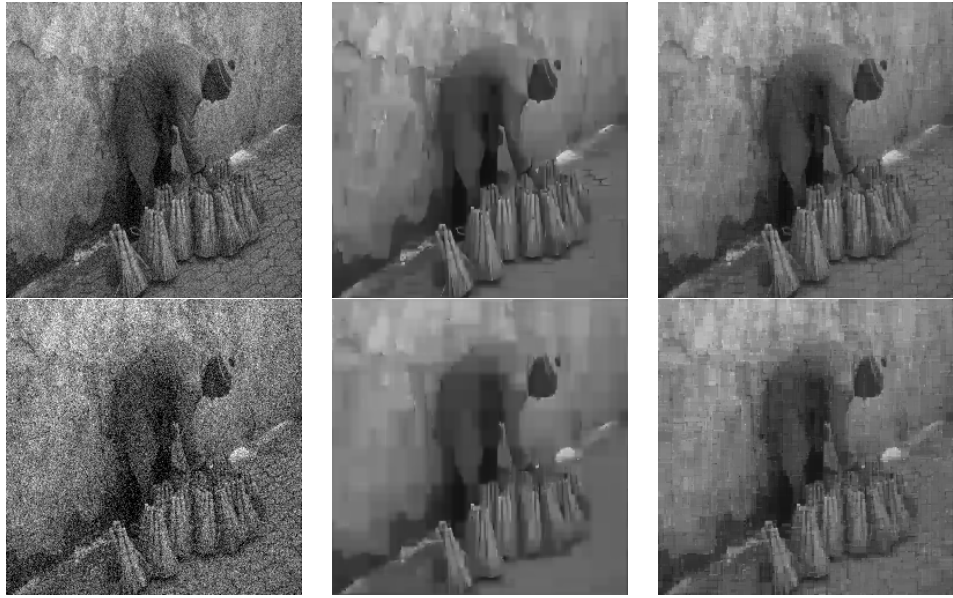


Figure 9: Image 293029 from the BSDS data set. **Top row:** Left: image with noise standard deviation  $0.2 \times \text{sd}(\text{image})$ . Center: image denoised by BMA with cycle-spinning step=2 (MSE =  $1.55 \times 10^3$ ). Right: image denoised by boosting with prune 0.2 and learning rate 0.05 (MSE =  $1.32 \times 10^3$ ). **Third row:** Left: image with noise standard deviation  $0.4 \times \text{sd}(\text{image})$ . Center: image denoised by BMA with cycle-spinning step=2 (MSE =  $2.34 \times 10^3$ ). Right: image denoised by boosting with prune 0.2 and learning rate 0.05 (MSE =  $2.20 \times 10^3$ ).

to the estimators rather than to the noise-generation artifact.

## L.2 Numerical results for tensor

We conduct an empirical study to evaluate the performance of unbalanced Haar (UH) partitioning methods extended to three-dimensional tensor domains. Here we consider a discrete, regular grid  $\Omega \subset \mathbb{R}^3$  with dimensions  $64 \times 64 \times 64$ , representing a video sequence. The clean video tensor signal  $f: \Omega \rightarrow \mathbb{R}$  is corrupted by additive i.i.d. Gaussian noise  $\varepsilon \sim \mathcal{N}(0, \sigma^2)$  where  $\sigma = 0.1 \cdot \text{std}(f)$ , yielding the observed tensor  $y = f + \varepsilon$ . For tensor decision tree methods, we extract overlapping patches of size  $2 \times 2 \times 1$ , generating  $N = (62) \times (62) \times (64) = 248832$  training samples.

The evaluation encompasses three reconstruction approaches. The first follows the standard Gibbs-style backfitting, implementing single-step proposals per component with  $K = 200$  additive terms 500 backfitting iterations. The second utilizes a patch-based regression framework using `TensorDecisionTreeRegressor` (Luo et al. 2025) as weak learners with maximum depth of 3 within a boosting ensemble of  $M = 50$  estimators, where reconstruction proceeds by averaging overlapping patch predictions. The third is a single `TensorDecisionTreeRegressor` learner.

The quality of a reconstructed tensor  $\hat{f}$  relative to the clean signal  $f$  is assessed via mean squared error:  $\text{MSE} = \mathbb{E}[\|f - \hat{f}\|_2^2]$ . Figure 11 illustrates the reconstruction performance across temporal slices. The best performance is achieved by the boosted ensemble of

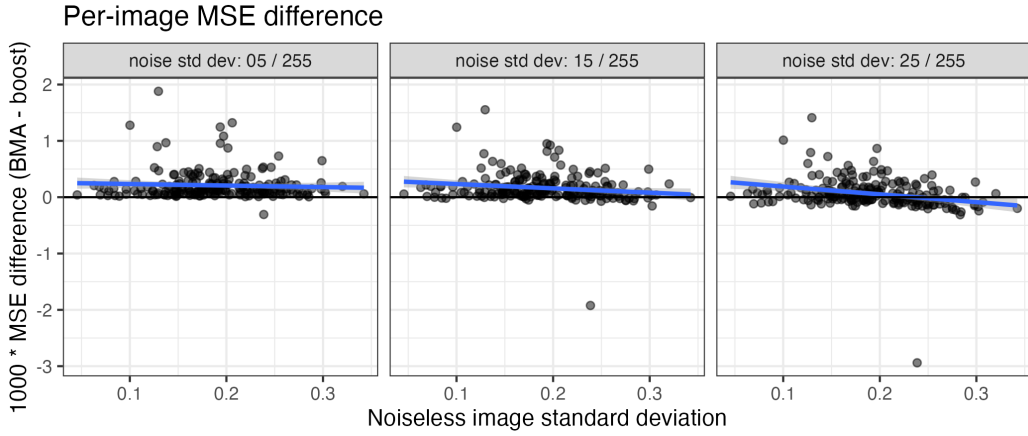


Figure 10: Per-image test MSE difference between BMA with one cycle-spinning step and boosting with  $b = 0.2$ . Each point corresponds to a BSDS image.

TensorDecisionTreeRegressors. This is perhaps expected, seeing as these weak learners use tensor-specific technology. In contrast, UHWTs are not tensor specific, and still the backfitting ensemble of UHWTs achieves good performance as well. Interestingly, the reconstruction by the boosted ensemble looks to be a bit blurry, whereas the reconstruction by the backfitting ensemble is crisper but does not denoise as well. Ensembling seems necessary to achieve a satisfactory MSE, seeing as the single TensorDecisionTreeRegressor learner produces an MSE that is at least five times either of those by the ensemble models.

Figure 12 demonstrates the uncertainty quantification capabilities inherent in the Bayesian framework. The posterior mean provides a denoised reconstruction, while the posterior standard deviation  $\sigma$  reveals regions of higher uncertainty, particularly along boundaries and in areas with complex geometric features. The 95% credible interval width offers additional insight into reconstruction confidence, with narrower intervals in homogeneous regions and wider intervals in areas where the model exhibits greater uncertainty. This uncertainty quantification proves valuable for assessing reconstruction reliability and identifying regions requiring additional modeling attention.

This evaluation confirms the viability of extending UH partitioning to higher-dimensional tensor domains while highlighting the trade-offs between single adaptive partitions versus additive ensemble strategies for tensor reconstruction tasks.

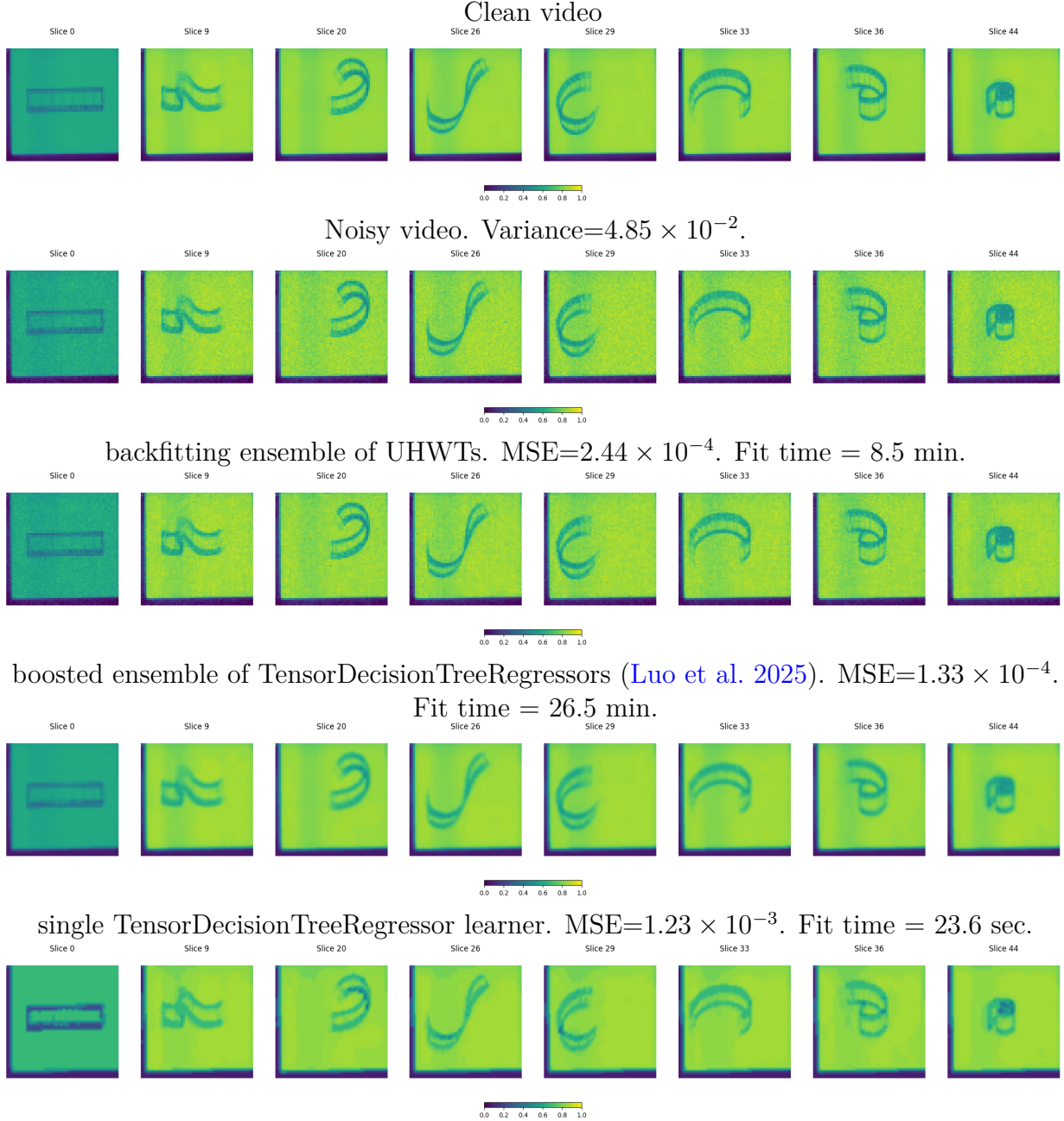


Figure 11: Temporal slice comparison demonstrating video denoising performance. Row 1: ground truth clean video frames showing temporal evolution of the underlying signal structure. Row 2: noisy observations with additive Gaussian noise ( $\sigma = 0.1 \cdot \text{std}(f)$ ). Row 3: reconstructed frames using a backfitting ensemble of 200 weak UH learners. Row 4: reconstructed frames using a boosted ensemble of 50 weak TensorDecisionTreeRegressor learners. Row 5: a single TensorDecisionTreeRegressor learner.

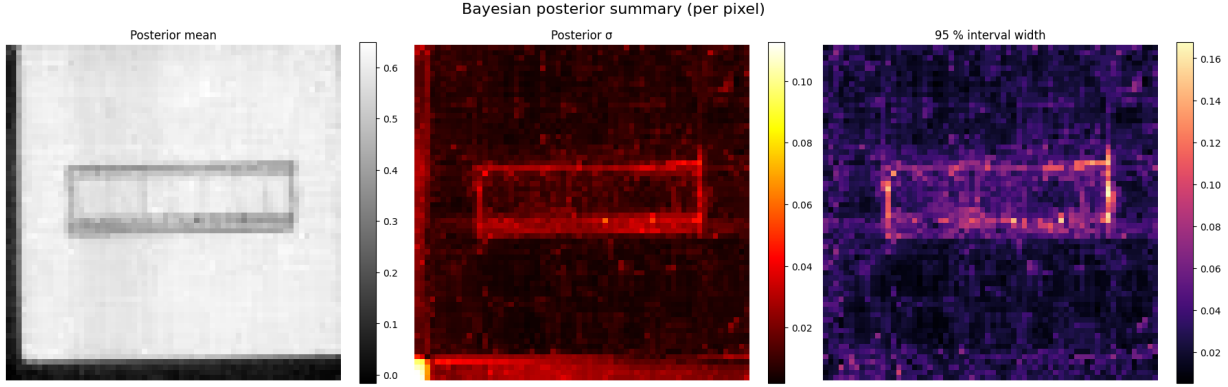


Figure 12: Bayesian uncertainty quantification for tensor reconstruction (slice 0). Left: Posterior mean estimate providing the denoised reconstruction. Center: Posterior standard deviation revealing spatially-varying uncertainty, with higher values (red/yellow regions) indicating areas where the model exhibits greater reconstruction uncertainty, particularly along object boundaries and complex geometric features. Right: Width of 95% credible intervals, offering pixel-wise confidence assessment with narrower intervals (dark blue) in homogeneous regions and wider intervals (yellow) in structurally complex areas.

### L.3 Numerical results for sphere

#### L.3.1 Simulation experiment 1: bias-variance analysis

In a Random Forest framework, our fitted spherical wavelet trees are essentially identical, and so the ensemble’s variance will not be reduced by model averaging (as seen by the roughly constant test MSE); in this case, the random rotations provide a much-needed decorrelation between learners as seen by the large difference in test MSE between the rotated and non-rotated RF ensembles using our fitted spherical wavelet trees, but the test MSE lower bound of  $\approx 0.4$  leaves room for improvement. In contrast, a non-rotated Fréchet tree can split away from the midpoint and hence already produces fairly uncorrelated learners; in this case, the ensemble’s variance is sharply reduced by model averaging, but the test MSE fails to fall below 0.2, which indicates the ensemble’s bias that the averaging process cannot reduce. The random rotations, which are independent of each other and of the data, slightly worsen the test MSE of the non-rotated Fréchet Forest. If the learners are truly uncorrelated, then the ensemble’s variance shrinks to zero as the number of learners increases, regardless of the base learner’s variance. Hence, the increased test MSE must come from an increase in the ensemble’s bias, which itself equals each base learner’s bias. Thus, we conclude that each random rotation increases both the bias and variance of the base learner.

In a boosting framework, a non-rotated Fréchet tree can split away from the midpoint and hence already allows diversity between learners; in this case, the ensemble’s test MSE sharply decreases to  $\approx 0.18$  but plateaus after roughly 100 learners. However, the random rotations slightly worsen the test MSE of the non-rotated Fréchet boosted ensemble. Seeing as boosting is meant to reduce bias in the ensemble, the slightly larger test MSE seems to result from the increase in each base learner’s variance from the random rotations. In contrast, our fitted spherical wavelet trees intuitively do not produce much diversity between

learners due to splitting only at midpoints and hence would strongly benefit from the inter-learner diversity induced by random rotations, even at the cost of increased bias and variance in each base learner. This is reflected empirically in the substantial reduction in test MSE when random rotations are incorporated in a boosted ensemble using our fitted spherical wavelet tree as the base learner. Perhaps surprisingly, this ensemble achieves the smallest test MSE ( $\approx 0.15$ ) among all tested methods. (This includes the test MSEs for three residual deep GP models shown in Table MT-2, where we see that the smallest mean MSE is 0.182, and for the spherical GP model, whose test MSE was 0.477.) Furthermore, this ensemble seemingly can still improve if the number of learners were to increase beyond 500. In this scenario, for either base learner, boosting produced smaller test MSEs than did model averaging, which suggests that each learner's bias dominates its variance. In addition, a single spherical wavelet tree using `adapt` has a smaller variance and larger bias than a single Fréchet tree has, which makes it a more promising base learner in a boosting framework. As a bonus, it can be applied to generic topological triangulations and hence can be used for a larger class of input domains than can a Fréchet tree, which requires inputs to lie on a metric space.

### L.3.2 Simulation experiment 2: comparing splitting methods

Here we compare the impact of three splitting methods – `adapt`, `balance`, and `balance4` – on the empirical performance of a single-tree model per level-0 triangle and on a random-rotation boosted (RRB) ensemble of 500 trees per level-0 triangle. (The fourth – `adaptvertex` – takes too much training time.) Each comparison is for a given number of leaves per tree and a given test function from which training and test data, each of size  $N \in \{288, 990, 3870, 15300\}$ , are generated.

First we will compare the performance of the `adapt` and `balance` splitting methods. Figure 13 shows that the smallest test MSE is usually achieved by the `adapt` method, and it is achieved with 4 leaves per tree. In contrast, the `balance` method with 4 leaves per tree typically produces a larger test MSE, but once the number of leaves per trees is with least 8, the resulting test MSEs are comparable to the smallest test MSE achieved using the `adapt` method. Although training a tree with 8 leaves using the `balance` method is typically still a bit faster than training a tree with 4 leaves using the `adapt` method, we must also consider the storage cost: a tree with 8 leaves contains twice as much information as a tree with 4 leaves and hence requires twice as much memory to store. This is also an important consideration for speeding up any post-hoc operations on the tree, such as signal reconstruction.

Now we will compare against the `balance4` splitting method. For each of the latter two methods (for the  $N \geq 990$  cases), we see that the respective test MSE curve exhibits a U-shape due to the bias-variance trade-off: as tree depth increases, the ensemble increasingly adapts to the data but also increasingly risks overfitting. Due to the steepness of the dips, especially for larger  $N$ , it is important to choose the number of leaves per tree that minimizes the test MSE. However, this task is more difficult for the `balance4` method because there is less granularity in the choice of the number of leaves per tree; the number of leaves must be a power of 4 for the `balance4` method, whereas it must only be a power of 2 for the `adapt` and `balance` methods. In particular, the difference between 4 and 16 leaves per tree can

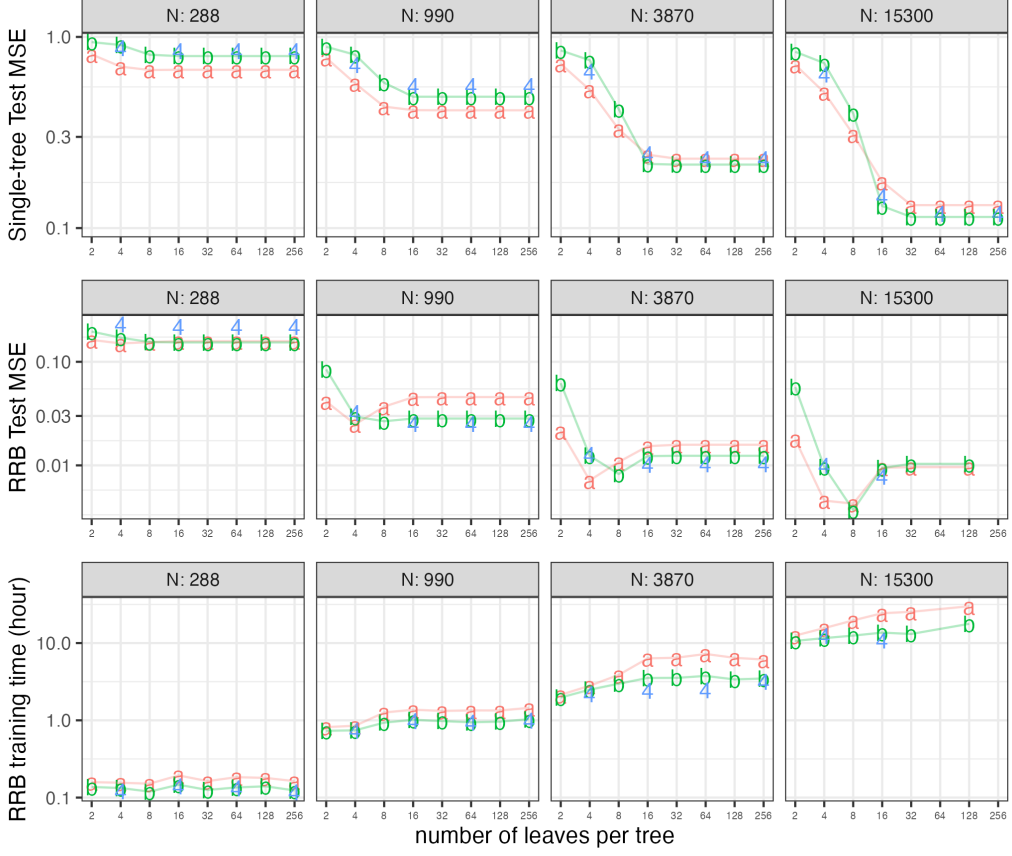


Figure 13: Empirical comparison of the impact of three splitting methods – `adapt` (‘a’), `balance` (‘b’), and `balance4` (‘4’) – on single-tree and random-rotation boosted models trained on  $N$  points  $(\mathbf{x}, y)$ , where each location  $\mathbf{x} = (x_1, x_2, x_3)$  was drawn uniformly on the unit sphere  $\mathbb{S}_2$ , and the observed response  $y$  at  $\mathbf{x}$  is the signal described in Figure MT-5 plus i.i.d. Gaussian noise with zero mean and standard deviation equal to 0.1 of the standard deviation of  $f$ . Boosted methods use learning rate 0.05.

have a significant impact on the test MSE, training time, and storage requirements. Hence, we argue that methods that split nodes into 2 children are favorable over methods that split nodes into 4 children.

### L.3.3 Simulation experiment 3: misaligned spherical features

Here, we consider a more complex benchmark function  $g$  for spherical functions. We want to validate the wavelet system on a spherical triangulation,  $g$  is a much better “structured yet controlled” test signal: intrinsic, oriented and slightly asymmetric (tilt) so we can spot real directional behavior rather than coordinate artifacts.

$$g(\mathbf{x}) = \sum_{i=1}^3 \left[ \exp\left(-\frac{(\mathbf{n}_i^\top \mathbf{x})^2}{\sigma_n^2}\right) + \beta \exp\left(-\frac{(\mathbf{n}_i^\top \mathbf{x})^2}{\sigma_w^2}\right) \right], \quad (90)$$

where the unit normals  $\{\mathbf{n}_i\}$  define three planes (one tilted) whose intersections with  $\mathbb{S}^2$  are great circles.

Both functions are useful. The baseline  $f$  defined in Figure MT-5 is simple, smooth, and inexpensive to evaluate, so it is well suited for pipeline checks and calibration. However, for fitting wavelets on a triangulated sphere,  $g$  is preferable for six reasons. First,  $g$  is intrinsic: since  $\mathbf{n}_i^\top \mathbf{x} = \cos \theta$ , it organizes energy by geodesic distance, whereas  $f$  depends on extrinsic coordinates. Second,  $g$  supplies multiple oriented features, enabling stringent tests of directional selectivity absent from  $f$ 's single dominant oscillation. Third,  $g$  provides localized multiscale content via narrow bands and diffused halos, unlike  $f$ 's broadly distributed trends. Fourth,  $g$  exposes mesh anisotropy because its features are uniform along geodesics, while  $f$  may align with grid directions. Fifth,  $g$  yields a balanced dynamic range with salient circle intersections that stabilize error metrics;  $f$ 's linear and saturating parts can overwhelm  $\cos(10x_2)$ . Sixth,  $g$  contains curvilinear singular structures that are harder than the near-band-limited behavior of  $f$ , thereby offering a more discriminative benchmark for spherical wavelets.

As mentioned in the main text, the prediction and MSE behaviors (shown in Figure 14) are similar to those for the signal described in Figure MT-5. Interestingly, here the residual deep GP models (MSEs in Table 5) fare much better. In fact, the test MSE ( $0.0374 \pm 0.0030$ ) of the best performing GP model (1 layer with inducing points, so it is not a deep GP) is smaller than all but the random-rotation boosted ensemble's (0.0330). We also note that it appears that increasing the number of ensembles will further decrease the test MSE for the random-rotation boosted ensemble, whereas there is no clear path for improvement for the GP model with inducing points.

### L.3.4 Simulation experiment 4: irregular benchmark function

Here, we consider an “irregular” benchmark function for spherical functions as described in Figure 4a of [Wyrwal et al. \(2025\)](#). The prediction and MSE behaviors, shown in Figure 15, are similar to those for the signal described in Figure 14. Again, here the residual deep GP models produce competitive test MSEs; the test MSE ( $1.657 \pm 0.027 \times 10^{-3}$ ) of the best performing GP model is smaller than all but the random-rotation boosted ensemble's ( $1.514 \times 10^{-3}$  with 1500 learners, not shown). We also note that even after 1500 learners, the random-rotation boosted ensemble's test MSE looks like it will further decrease as the number of learners increases. At 1500 learners, this test MSE is smaller than any of the deep GP MSEs shown in Table 6.

### L.3.5 Uncertainty quantification on a spherical domain

Here we apply a frequentist approach to uncertainty quantification (UQ) on the GISS data from Section MT-6.3. In Figure 16, we also provide predictive UQ by adapting the approach in quantile regression forests ([Meinshausen & Ridgeway 2006](#)) to our random-forest ensemble of  $B = 500$  spherical learners using `adapt`. This UQ method can be incorporated for Random Forest or Boosting (with or without random rotations), but because the purpose is not necessarily to compare the UQ performance of various ensembles, we illustrate this UQ method for only one ensemble. For a query  $\mathbf{x}$ , a quantile regression forest provides

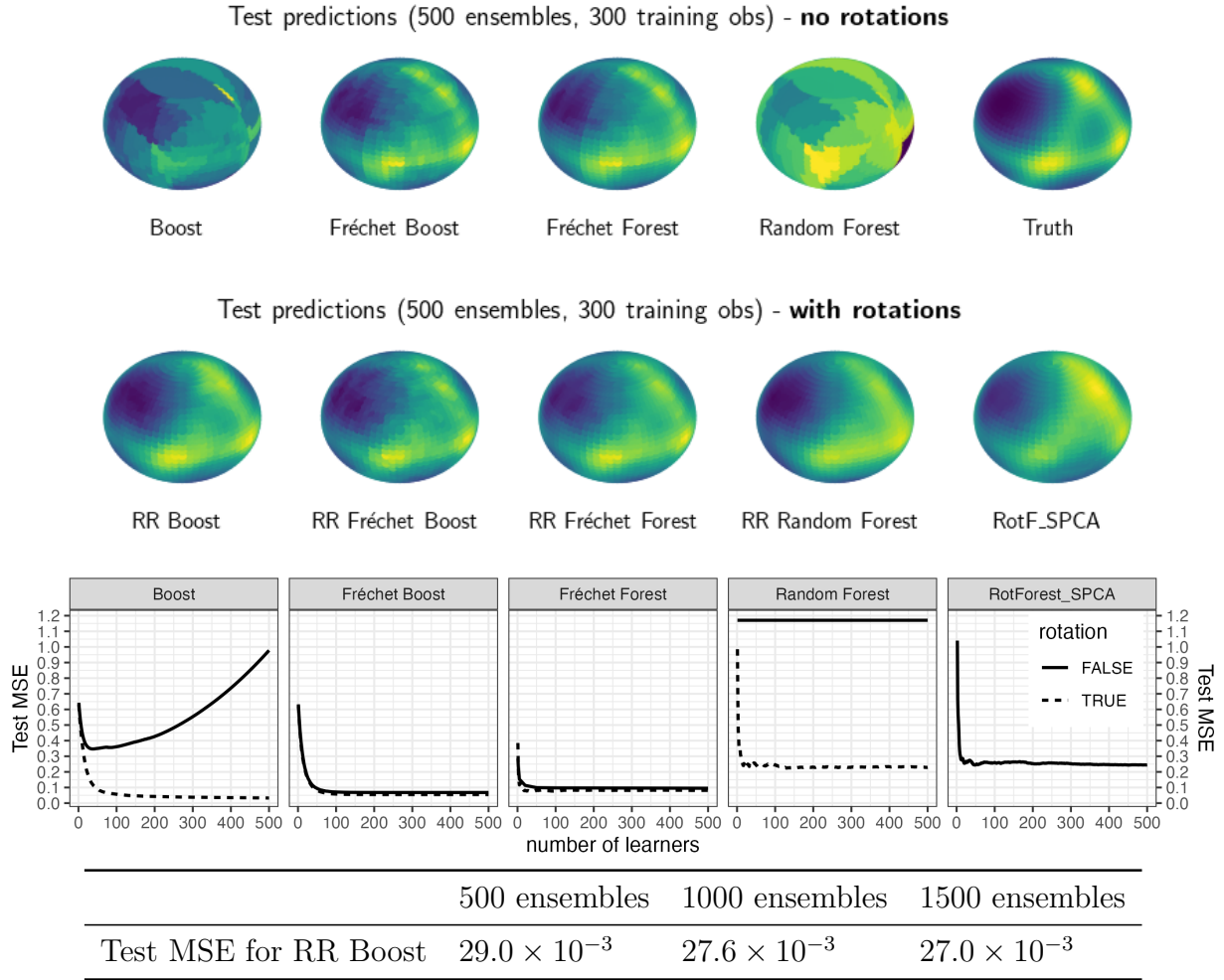


Figure 14: Empirical comparison of various tree ensemble models (“RR” refers to the method version that randomly rotates covariates before fitting any base learner) trained on  $n = 300$  points  $(\mathbf{x}, y)$ , where each location  $\mathbf{x} = (x_1, x_2, x_3)$  was drawn uniformly on the unit sphere  $\mathbb{S}_2$ , and the observed response  $y$  at  $\mathbf{x}$  is the signal  $f(\mathbf{x}) = \exp\{-16x_3^2\} + 1.5 \exp\{-16x_3^2/9\} + \exp\{-16x_2^2\} + 1.5 \exp\{-16x_2^2/9\} + \exp\{-16n(\mathbf{x})\} + 1.5 \exp\{-16n(\mathbf{x})/9\}$ , where  $n(\mathbf{x}) = [x_1 \cos(35^\circ) - x_2 \sin(35^\circ) + x_3 \sin(35^\circ)]^2$  plus i.i.d. Gaussian noise with zero mean and standard deviation equal to 0.1 of the standard deviation of  $f$ . The true signal is shown in the right-most sphere of the top row. All tree-based methods allow trees to grow to full depth. Boosted methods use learning rate 0.05. Top two rows: predictions of the ensemble methods. Third row: MSE on 2448 test points.

conditional quantiles by assigning to each training index  $(i = 1, \dots, n)$  the weight

$$w_i(\mathbf{x}) = \frac{1}{B} \sum_{b=1}^B \sum_{A \in \mathcal{L}(T_b)} \frac{\mathbf{1}\{\mathbf{x}_i \in A\} \mathbf{1}\{\mathbf{x} \in A\}}{|\{j: \mathbf{x}_j \in A\}|},$$

where  $\mathcal{L}(T)$  denotes the set of leaf nodes in tree  $T$ , and then inverting the weighted empirical cumulative distribution function  $\hat{F}_{Y|X=x}(t) = \sum_{i=1}^n w_i(x) \mathbf{1}\{y_i \leq t\}$ .

Test MSE for residual deep GP	1 layer	2 layers	3 layers	4 layers
+hodge+spherical_harmonic_features	<b>52.7 (0)</b>	53.1 (0.1)	53.1 (0.1)	53.2 (0.1)
+inducing_points	<b>37.4 (3.0)</b>	53.1 (16.5)	52.9 (16.2)	52.6 (15.2)
+spherical_harmonic_features	<b>52.7 (0)</b>	53.6 (0.1)	53.8 (0.1)	53.8 (0.1)

Table 5: Mean and standard deviation of test MSE ( $\times 10^{-3}$ ) for three residual deep GP methods (Wyrwal et al. 2025) over 10 starting seeds. Data were generated as described in Figure 14. Smallest test MSE for each method is bolded.

Test MSE for residual deep GP	1 layer	2 layers	3 layers	4 layers
+hodge+spherical_harmonic_features	3.078 (0)	2.555 (0.582)	2.511 (0.473)	<b>2.424 (0.579)</b>
+inducing_points	3.078 (0)	1.716 (0.075)	<b>1.662 (0.025)</b>	<b>1.663 (0.027)</b>
+spherical_harmonic_features	3.078 (0)	1.769 (0.205)	<b>1.657 (0.027)</b>	1.677 (0.063)

Table 6: Mean and standard deviation of test MSE ( $\times 10^{-3}$ ) for three residual deep GP methods (Wyrwal et al. 2025) over 10 starting seeds. Data were generated as described in Figure 15. Smallest test MSE for each method is bolded.

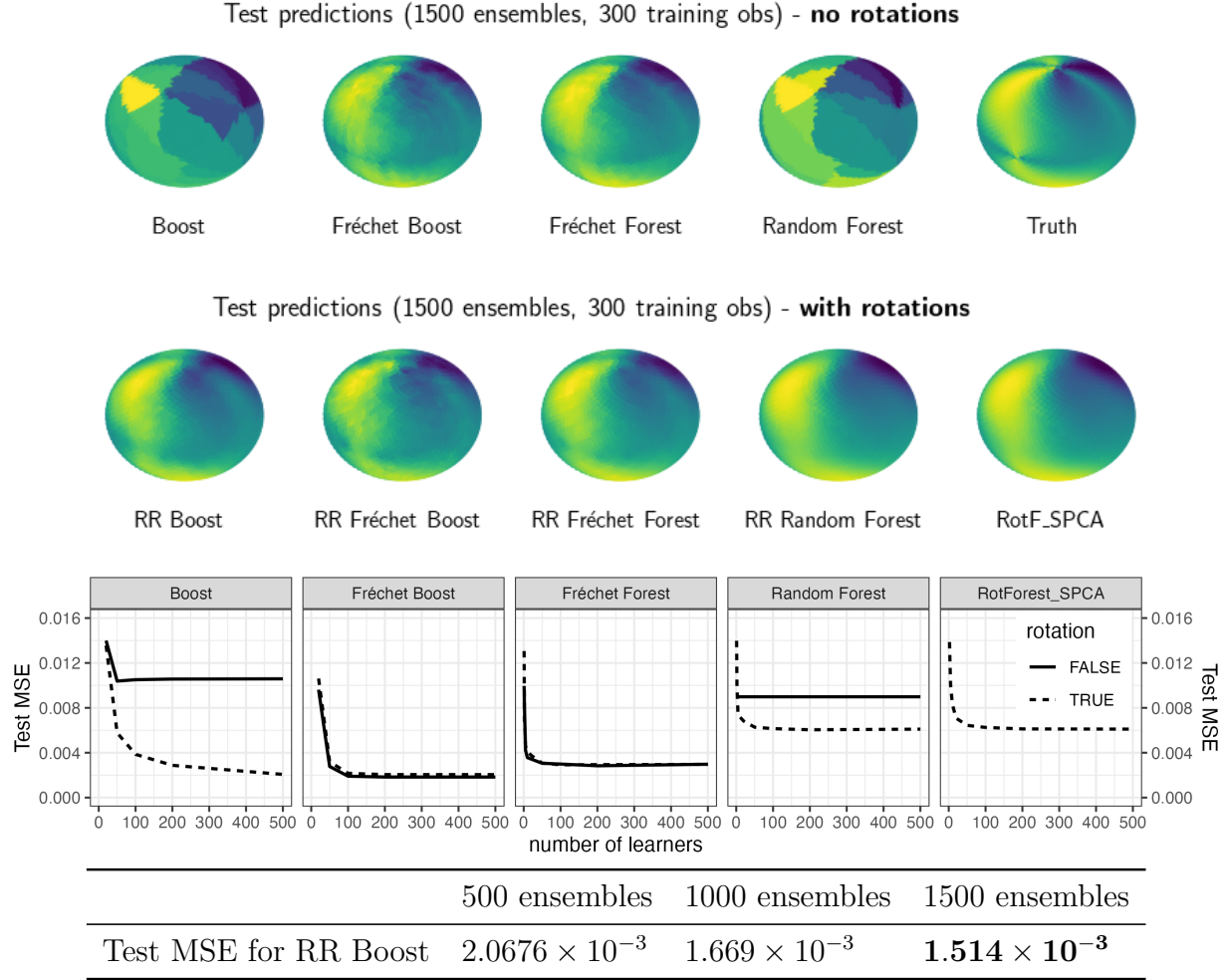


Figure 15: Empirical comparison of various tree ensemble models (“RR” refers to the method version that randomly rotates covariates before fitting any base learner) trained on  $n = 300$  points  $(\mathbf{x}, y)$ , where each location  $\mathbf{x} = (x_1, x_2, x_3)$  was drawn uniformly on the unit sphere  $\mathbb{S}_2$ , and the observed response  $y$  at  $\mathbf{x}$  is the signal described in Figure 4a of [Wyrwal et al. \(2025\)](#) plus i.i.d. Gaussian noise with zero mean and standard deviation equal to 0.1 of the standard deviation of  $f$ . The true signal is shown in the right-most sphere of the top row. All tree-based methods allow trees to grow to full depth. Boosted methods use learning rate 0.05. Top two rows: predictions of the ensemble methods. Third row: MSE on 2448 test points.

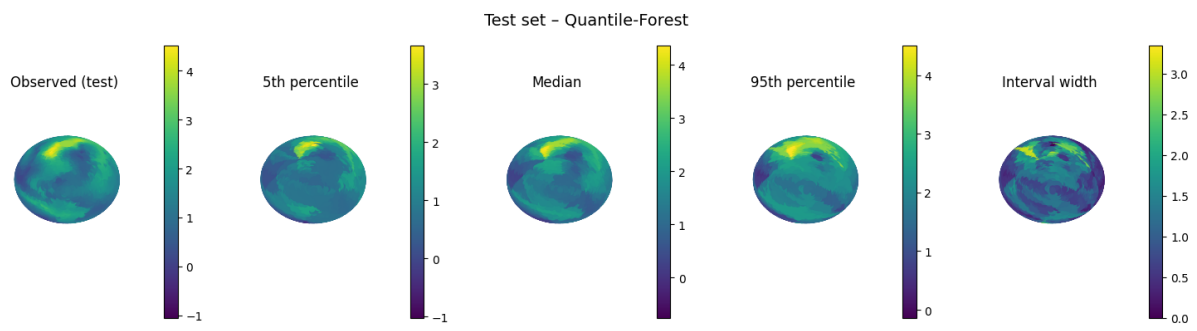


Figure 16: Quantile predictions of a Random Forest of 500 spherical learners per initial triangle using `adapt` trained data described in Figure MT-6. This ensemble achieved an empirical 90% coverage of 87.7%.